CSIAM Trans. Appl. Math.
doi: 10.4208/csiam-am.SO-2023-0021

Vol. **x**, No. x, pp. 1-39
xx 2024

Total Variations for Hue, Saturation, and Value of a Color Image

Wei Wang* and Chengyun Yang

School of Mathematical Sciences, Key Laboratory of Intelligent Computing and Applications (Ministry of Education), Tongji University, Shanghai 200092, P.R. China.

Received 23 May 2023; Accepted 19 March 2024

Abstract. In this paper, we develop total variations for hue, saturation, and value of a color image, and we propose a novel hue-saturation-value total variation model for color image restoration. We first refine the hue formulation of a color image to make it mathematically and applicationally meaningful by assigning different hue values to different colors. We then develop the proposed hue-saturation-value total variation based on the conception of hue/saturation/value gradient. We investigate the dual formulation and the properties of the proposed hue-saturation-value total variation, and we finally propose a color image restoration model which is formulated by combing the proposed hue-saturation-value total variation regularization with the data-fitting term between the objective color image and the observed color image. We develop an efficient alternating iterative algorithm to solve the proposed optimization model in practice, and we give the convergence analysis of the proposed algorithm. Numerical examples are presented to demonstrate that the performance of the proposed hue-saturation-value total variation and the proposed color restoration model is better than that of other testing methods in terms of visual quality, peak signal-to-noise ratio (PSNR), structural similarity index (SSIM), and S-CIELAB color error.

AMS subject classifications: 65K10, 65J22, 68U10, 90C26

Key words: Total variation, color image restoration, hue, saturation, value, alternating iterative algorithm.

1 Introduction

The representation ways of color images have been extensively developed [5]. One of the most popular color representation models is RGB (red, green, blue) color space, which

*Corresponding author. *Email addresses:* wangw@tongji.edu.cn (W. Wang), 2211185@tongji.edu.cn (C. Yang)

is the most general hardware-oriented model. Another widely used color space is HSV (hue, saturation, value) color space, which is similar to human color perception. In the literature, many color image processing models are proposed based on different color spaces, e.g. color image restoration [2, 4, 9, 13, 28, 30, 36], color image enhancement [9, 15] based on RGB color space, color image restoration [8], color image segmentation [10, 20, 39] based on HSV color space, color image restoration [22], color image enhancement [1] based on CIELAB color space, color image enhancement [33], color image restoration [19, 21, 23, 25, 32, 34], color image decomposition [26, 37] based on opponent color space, etc.

Images will be affected by the interference of imaging equipment and external environment noise during digitizing and transmitting. Therefore, regularization methods need to be designed to deal with image restoration problem. As one of the most popular regularization methods, total variation (TV) [29] is proposed to deal with grayscale images, and has been developed into many other forms for handling corresponding image processing problems. For instance, anisotropic TV [14] is designed for image decomposition problem, and nonlocal TV [16, 31] makes use of image structures and features for image restoration problem. On the other hand, TV regularization is also generalized for vector-valued (color of multichannel) image regularization. Bresson and Chan [4] proposed a color TV regularization with a local channel-coupling

$$\text{C-TV}(\mathbf{u}) := \int_\Omega \sqrt{\sum_{k=1}^{c} \big(\partial_x u_k(x,y)\big)^2 + \big(\partial_y u_k(x,y)\big)^2}\, dxdy,$$

where Ω is the image domain, c is the number of channels, $u_k(x,y)$ is the k-th channel of vector-valued image $\mathbf{u} = [u_1(x,y), u_2(x,y), \cdots, u_c(x,y)]^\top$ and $\partial_x u_k$ (or $\partial_y u_k$) is the partial derivative of u_k with respect to x (or y). In [13], the comparison of the TV regularization with the local-channel coupling C-TV and the global channel coupling C-TV has been studied, which shows that C-TV can determine edge locations in different channels. Moreover, Duran *et al.* [13] studied the gradient of a multispectral image as a three-dimensional (3D) matrix or tensor with the dimensions corresponding to the spatial and spectral channels. Different norms along different dimensions can be employed to measure the smoothness of this tensor. Paul *et al.* [28] proposed the generalized vector-valued total variation (GV-TV) by coupling different channels with different norms. We remark here that many efficient algorithms can be applied to solve different vectorial total variation models, such as the augmented Lagrangian method [18,27,38], dual method [6,7,38], the split Bregman algorithm [3,38] and the iteratively reweighted norm algorithm [28].

Color images can be studied from the view of Riemann geometry. In [12], a vector-valued image was considered as a parametric 2D manifold embedded in a C-dimensional space, where C is the number of channels. One idea is to study the spectral information of $(\nabla \mathbf{u}(x,y))^\top \nabla \mathbf{u}(x,y)$, which refers to the structure tensor of the image. The spectral information would be useful for describing edges of color images. Sapiro [30] proposed the following vectorial TV model:

$$\text{V-TV}(\mathbf{u}) := \int_\Omega \varphi\big(\lambda^+(x,y), \lambda^-(x,y)\big)\, dxdy,$$

where λ^+, λ^- correspond to the eigenvalues of the eigenvectors of $(\nabla \mathbf{u}(x,y))^\top \nabla \mathbf{u}(x,y)$, and $\varphi(\cdot)$ is a penalty function. Many forms of $\varphi(\cdot)$ can be defined to describe the edges of color images, for example, by choosing Schatten-∞ norm (also noted as V-TV)

$$\text{V-TV}(\mathbf{u}) := \int_\Omega \sqrt{\lambda^+(x,y)}\, dxdy.$$

This form can be used to penalize the largest gradient change in $\nabla \mathbf{u}(x,y)$. $\varphi(\cdot)$ can also be defined as the Frobenius norm or p-norm, see details in [17].

Besides different kinds of geometric models, another useful technique in color image processing is to transform color images to other color spaces. Chan *et al.* [8] studied the TV image restoration based on the chromaticity-brightness model and the HSV model. The idea is to apply TV regularization on the objective image in the transformed color space, e.g. applying TV denoising procedure to the chromaticity component (or hue component and saturation component) and the brightness component separately. In [11], the opponent color space, which is an equivalent version of HSV color space, was proposed by using quaternion framework, and Jia *et al.* [21] proposed the saturation-value total variation (SV-TV) model based on HSV color space in quaternion framework

$$\text{SV-TV}(\mathbf{u}) := \int_\Omega \sqrt{|\partial_x \mathbf{u}(x,y)|_s^2 + |\partial_y \mathbf{u}(x,y)|_s^2} + \alpha \sqrt{|\partial_x \mathbf{u}(x,y)|_v^2 + |\partial_y \mathbf{u}(x,y)|_v^2}\, dxdy,$$

where $|\cdot|_s$ and $|\cdot|_v$ mean the saturation component and value component, α is a parameter for balancing the saturation regularization and value regularization. Notice that the proposed SV-TV model in [21] make use of the saturation regularization to eliminate the color disturbance, and make use of the value regularization to remove the value artifacts. However, SV-TV model does not consider the information of the hue component, which may lead to unexpected color loss during SV-TV based color image processing.

In this paper, we develop total variations for hue, saturation, and value of a color image, and we propose a novel hue-saturation-value total variation model for color image restoration. We first reconstruct the HSV color space by using quaternion framework. We then refine the hue representation to make it mathematically and applicationally meaningful by assigning different hue values to different colors. We finally propose and develop a novel hue-saturation-value total variation (HSV-TV) regularization method based on the conception of hue/saturation/value gradient. We investigate the dual formulation and the properties of the proposed hue-saturation-value total variation. Color image restoration model is then formulated by combing the proposed HSV-TV regularization method with the data-fitting term between the objective color image and the observed color image. We develop an efficient alternating iterative algorithm to solve the proposed optimization model in practice, and we give the convergence analysis of the proposed algorithm. Numerical examples are presented to demonstrate that the performance of the proposed hue-saturation-value total variation and the proposed HSV-TV color restoration model is better than that of other testing methods in terms of visual quality, peak

signal-to-noise ratio (PSNR), structural similarity index (SSIM) [35], and S-CIELAB color error [40].

The outline of this paper is given as follows. In Section 2, we reconstruct the HSV color space by using quaternion framework, and refine the hue formulation. In Section 3, we introduce the hue-saturation-value total variation and the proposed color image restoration model, meanwhile, we give the theoretical analysis of the proposed HSV-TV approach. In Section 4, we present an efficient alternating iterative algorithm to solve the proposed color image restoration model. In Section 5, we report numerical examples to demonstrate the effectiveness of the proposed approach. Finally, some concluding remarks are given in Section 6.

2 Hue, saturation, and value of a color image

2.1 Hue, saturation, value, and quaternion

In this subsection, we will give the expressions of hue, saturation, and value in the quaternion framework. We first quote two lemmas in [11,26] for quaternion calculations.

Lemma 2.1. *If* $\mathbf{p},\mathbf{q}$ *are two pure quaternions (which are equivalent to three-dimensional vectors), then*

$$\mathbf{pq}=\mathbf{p}\times\mathbf{q}-\mathbf{p}\cdot\mathbf{q}.$$

Moreover, if $\mathbf{p},\mathbf{q}$ *are still orthogonal, then*

$$\mathbf{pq}=\mathbf{p}\times\mathbf{q},$$

where $\mathbf{p}\times\mathbf{q}$ *means the cross product of* $\mathbf{p}$ *and* $\mathbf{q}$ *as three-dimensional vectors.* $\mathbf{p}\cdot\mathbf{q}$ *means the scalar product of* $\mathbf{p}$ *and* $\mathbf{q}$ *as three-dimensional vectors.*

Lemma 2.2. *If* $\mathbf{u},\boldsymbol{\mu}$ *are two pure quaternions, and* μ *is unitary, then*

- *The reflection of* $\mathbf{u}$ *with respect to* $\boldsymbol{\mu}$ $(\mathbf{u}^{\boldsymbol{\mu}}_{refl}=-\boldsymbol{\mu}\mathbf{u}\boldsymbol{\mu})$ *is the reflection vector of* $\mathbf{u}$ *onto* $\boldsymbol{\mu}$.
- *The projection of* $\mathbf{u}$ *with respect to* $\boldsymbol{\mu}$ $(\mathbf{u}^{\boldsymbol{\mu}}_{proj}=(\mathbf{u}-\boldsymbol{\mu}\mathbf{u}\boldsymbol{\mu})/2)$ *is the projection vector of* $\mathbf{u}$ *onto* $\boldsymbol{\mu}$.
- *The rejection of* $\mathbf{u}$ *with respect to* $\boldsymbol{\mu}$ $(\mathbf{u}^{\boldsymbol{\mu}}_{rej}=(\mathbf{u}+\boldsymbol{\mu}\mathbf{u}\boldsymbol{\mu})/2)$ *is the projection vector of* $\mathbf{u}$ *onto the orthogonal plane of* $\boldsymbol{\mu}$.

Assume $\mathbf{u}=(u_r,u_g,u_b)$ is a color image defined on an image domain Ω. Then $\mathbf{u}(x,y)$ can be equivalently considered as a pure quaternion, i.e. $\mathbf{u}=u_r\mathtt{i}+u_g\mathtt{j}+u_b\mathtt{k}$. In Fig. 1, we show the projection vectors and the rejection vector of a color image $\mathbf{u}$ with respect to the axis of a cone coordinate system built based on the quaternion calculations. The following theorem gives the expressions of the hue, saturation, and value components of $\mathbf{u}$ in the quaternion framework.

Theorem 2.1. *The hue, saturation, and value components of a color image* $\mathbf{u}$ *is given as follows in the quaternion framework:*

$$\begin{cases} c_h(x,y) = \tan^{-1}\left(\dfrac{|\mathbf{u}(x,y)+\mu\nu\mathbf{u}(x,y)\nu\mu|}{|\mathbf{u}(x,y)-\nu\mathbf{u}(x,y)\nu|}\right), \\ c_s(x,y) = \dfrac{1}{2}|\mathbf{u}(x,y)+\mu\mathbf{u}(x,y)\mu|, \\ c_v(x,y) = \dfrac{1}{2}|\mathbf{u}(x,y)-\mu\mathbf{u}(x,y)\mu|, \end{cases}$$

where μ *is the gray-value axis and* ν *is a reference color which is unitary and orthogonal to* μ.

Proof. First, we set $\gamma = \mu\nu$. By applying Lemma 2.1, we can easily derive that γ is orthogonal to the plane determined by μ and ν. Recall that a color vector in HSV color space can be considered as a point in a cone from a geometric point of view. We then make use of γ, μ, and ν to build a cone in the quaternion framework. As is shown in Fig. 1, the main idea is to choose μ as the central axis. Then the value component of a color $\mathbf{u}$ is the length of the projection of $\mathbf{u}$ onto μ. The saturation component is the length of the rejection of $\mathbf{u}$ onto μ. The hue component is the angle between the reference color ν and the rejection of $\mathbf{u}$ onto μ, which can be described by using the value of the arc tangent function at the ratio of the projection length of $\mathbf{u}$ onto γ to the projection length of $\mathbf{u}$ onto ν. Combining the calculations in Lemma 2.2, we can easily deduce that the formulations of c_h, c_s, and c_v based on the quaternion framework are given as follows:

$$c_h = \tan^{-1}\left(\frac{|\mathbf{u}^{\gamma}_{proj}|}{|\mathbf{u}^{\nu}_{proj}|}\right) = \tan^{-1}\left(\frac{|\mathbf{u}-\gamma\mathbf{u}\gamma|}{|\mathbf{u}-\nu\mathbf{u}\nu|}\right) = \tan^{-1}\left(\frac{|\mathbf{u}+\mu\nu\mathbf{u}\nu\mu|}{|\mathbf{u}-\nu\mathbf{u}\nu|}\right),$$

$$c_s = |\mathbf{u}^{\mu}_{rej}| = \frac{1}{2}|\mathbf{u}+\mu\mathbf{u}\mu|, \quad c_v = |\mathbf{u}^{\mu}_{proj}| = \frac{1}{2}|\mathbf{u}-\mu\mathbf{u}\mu|.$$

The proof is complete. □

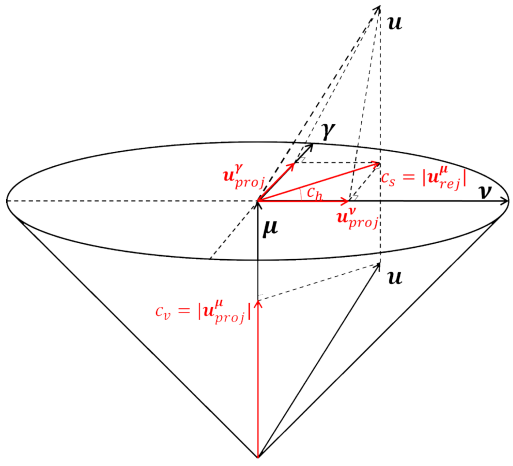

Figure 1: The geometric meaning of HSV in the quaternion framework.

2.2 Hue, saturation, and value of a color image

In this subsection, we will further study the representations of hue, saturation, and value for a color image. We will establish the conversion relationship between red, green, blue and quaternion based hue, saturation, value, meanwhile, we will try to figure out how different couplings between red, green, and blue channels describe different features (hue, saturation, value) of a color image.

In the following discussion, we set $\boldsymbol{\mu}=(\mathtt{i}+\mathtt{j}+\mathtt{k})/\sqrt{3}$ corresponding to the grey-value axis. Noting that $\boldsymbol{\nu}$ is a reference color which is unitary and orthogonal to $\boldsymbol{\mu}$. In this paper, we choose the reference color $\boldsymbol{\nu}$ corresponding to the red color $\mathtt{i}$. By using Lemma 2.2, $\boldsymbol{\nu}$ can be calculated as follows:

$$\boldsymbol{\nu}=\frac{(\mathtt{i}+\boldsymbol{\mu}\mathtt{i}\boldsymbol{\mu})/2}{|(\mathtt{i}+\boldsymbol{\mu}\mathtt{i}\boldsymbol{\mu})/2|}=\frac{1}{\sqrt{6}}(2\mathtt{i}-\mathtt{j}-\mathtt{k}).$$

Then we can derive the representations of hue, saturation, and value based on the couplings of red, green, blue channels by using the quaternion calculations in Theorem 2.1. We conclude them in the following theorem.

Theorem 2.2. *Assume* $\mathbf{u}=(u_r,u_g,u_b)^\top$ *is a color image. Then hue, saturation, and value of* $\mathbf{u}$ *can be give as*

$$\mathrm{H}(\mathbf{u})=\tan^{-1}\left(\frac{\|\mathbf{C_1u}\|}{\|\mathbf{C_2u}\|}\right),\quad \mathrm{S}(\mathbf{u})=\|\mathbf{Cu}\|,\quad \mathrm{V}(\mathbf{u})=\frac{1}{\sqrt{3}}|u_r+u_g+u_b|,$$

where

$$\mathbf{C_1}=\begin{bmatrix}0&0&0\\0&1/2&-1/2\\0&-1/2&1/2\end{bmatrix},\quad \mathbf{C_2}=\begin{bmatrix}2/3&-1/3&-1/3\\-1/3&1/6&1/6\\-1/3&1/6&1/6\end{bmatrix},\quad \mathbf{C}=\begin{bmatrix}2/3&-1/3&-1/3\\-1/3&2/3&-1/3\\-1/3&-1/3&2/3\end{bmatrix}.$$

Here, $\|\cdot\|$ *means the Frobenius norm of a three-dimensional vector.*

Proof. We first show some quaternion calculations as follows:

$$\begin{aligned}
&\mathbf{u}-\boldsymbol{\nu}\mathbf{u}\boldsymbol{\nu}=\frac{1}{3}\big((4u_r-2u_g-2u_b)\mathtt{i}+(-2u_r+u_g+u_b)\mathtt{j}+(-2u_r+u_g+u_b)\mathtt{k}\big),\\
&\frac{1}{2}|\mathbf{u}-\boldsymbol{\nu}\mathbf{u}\boldsymbol{\nu}|=\|\mathbf{C_2u}\|,\\
&\mathbf{u}+\boldsymbol{\mu}\boldsymbol{\nu}\mathbf{u}\boldsymbol{\nu}\boldsymbol{\mu}=(u_g-u_b)\mathtt{j}+(-u_g+u_b)\mathtt{k},\\
&\frac{1}{2}|\mathbf{u}+\boldsymbol{\mu}\boldsymbol{\nu}\mathbf{u}\boldsymbol{\nu}\boldsymbol{\mu}|=\|\mathbf{C_1u}\|,\\
&\mathbf{u}+\boldsymbol{\mu}\mathbf{u}\boldsymbol{\mu}=\frac{2}{3}\big((2u_r-u_g-u_b)\mathtt{i}+(-u_r+2u_g-u_b)\mathtt{j}+(-u_r-u_g+2u_b)\mathtt{k}\big),\\
&\frac{1}{2}|\mathbf{u}+\boldsymbol{\mu}\mathbf{u}\boldsymbol{\mu}|=\|\mathbf{Cu}\|,
\end{aligned}$$

$$\mathbf{u}-\boldsymbol{\mu}\mathbf{u}\boldsymbol{\mu}=\frac{2}{3}\big((u_r+u_g+u_b)\mathtt{i}+(u_r+u_g+u_b)\mathtt{j}+(u_r+u_g+u_b)\mathtt{k}\big),$$
$$\frac{1}{2}|\mathbf{u}-\boldsymbol{\mu}\mathbf{u}\boldsymbol{\mu}|=\frac{1}{\sqrt{3}}|u_r+u_g+u_b|.$$

By using the formulations of c_h, c_h, and c_h given in Theorem 2.1, we have

$$\mathrm{H}(\mathbf{u})=\tan^{-1}\left(\frac{\|\mathbf{C_1u}\|}{\|\mathbf{C_2u}\|}\right),\quad \mathrm{S}(\mathbf{u})=\|\mathbf{Cu}\|,\quad \mathrm{V}(\mathbf{u})=\frac{1}{\sqrt{3}}|u_r+u_g+u_b|.$$

The proof is complete. □

However, there is a problem with the definition of hue in Theorem 2.2, i.e. the range of $\mathrm{H}(\mathbf{u})$ is restricted in $[0,\pi/2]$, which causes confusion in color representation. Particularly, different colors may share the same hue. For example, let us check the hue of green $\mathbf{u_1}=(0,1,0)^T$ and blue $\mathbf{u_2}=(0,0,1)^T$ based on the formulation of $\mathrm{H}(\mathbf{u})$ as follows:

$$\mathbf{C_1u_1}=\begin{bmatrix}0\\1/2\\-1/2\end{bmatrix},\quad \mathbf{C_1u_2}=\begin{bmatrix}0\\-1/2\\1/2\end{bmatrix},\quad \|\mathbf{C_1u_1}\|=\|\mathbf{C_1u_2}\|=\frac{1}{\sqrt{2}},$$
$$\mathbf{C_2u_1}=\begin{bmatrix}-1/3\\1/6\\1/6\end{bmatrix},\quad \mathbf{C_2u_2}=\begin{bmatrix}-1/3\\1/6\\1/6\end{bmatrix},\quad \|\mathbf{C_2u_1}\|=\|\mathbf{C_2u_2}\|=\frac{1}{\sqrt{6}},$$

then it is easy to get that $\mathrm{H}(\mathbf{u_1})=\mathrm{H}(\mathbf{u_2})=\tan^{-1}(\sqrt{3})=\pi/3$. In order to deal with this problem, we further improve the formulation of hue in Definition 2.1.

Definition 2.1. *The formulation of hue is given as*

$$\mathrm{H}^*=\begin{cases}\mathrm{H}, & \beta_1>0,\quad \beta_2\geq 0,\\ \pi-\mathrm{H}, & \beta_1\leq 0,\quad \beta_2>0,\\ \pi+\mathrm{H}, & \beta_1<0,\quad \beta_2\leq 0,\\ 2\pi-\mathrm{H}, & \beta_1\geq 0,\quad \beta_2<0,\end{cases}\tag{2.1}$$

where

$$\beta_1=\mathrm{sign}\big((\mathbf{u}-\boldsymbol{\nu}\mathbf{u}\boldsymbol{\nu})\cdot\boldsymbol{\nu}\big)$$
$$=\begin{cases}1, & \mathbf{u}^{\nu}_{proj}\ \textit{and}\ \boldsymbol{\nu}\ \textit{are in the same direction},\\ 0, & \mathbf{u}^{\nu}_{proj}=0,\\ -1, & \mathbf{u}^{\nu}_{proj}\ \textit{and}\ \boldsymbol{\nu}\ \textit{in the opposite direction},\end{cases}$$

$$\beta_2 = \text{sign}\big((\mathbf{u}-\boldsymbol{\gamma}\mathbf{u}\boldsymbol{\gamma})\cdot\boldsymbol{\gamma}\big) = \text{sign}\big((\mathbf{u}+\boldsymbol{\mu}\boldsymbol{\nu}\mathbf{u}\boldsymbol{\nu}\boldsymbol{\mu})\cdot(\boldsymbol{\mu}\boldsymbol{\nu})\big)$$
$$= \begin{cases} 1, & \mathbf{u}^{\gamma}_{proj} \text{ and } \boldsymbol{\gamma} \text{ are in the same direction}, \\ 0, & \mathbf{u}^{\gamma}_{proj} = 0, \\ -1, & \mathbf{u}^{\gamma}_{proj} \text{ and } \boldsymbol{\gamma} \text{ are in the opposite direction}. \end{cases}$$

Noting that $\mathbf{u}^{\nu}_{proj} = (\mathbf{u}-\boldsymbol{\nu}\mathbf{u}\boldsymbol{\nu})/2$ *is the projection vector of* $\mathbf{u}$ *onto* $\boldsymbol{\nu}$*, then* β_1 *describes the direction of* $\mathbf{u}^{\nu}_{proj}$*. Similarly,* β_2 *describe the direction of* $\mathbf{u}^{\gamma}_{proj}$*. Finally, by letting* $\omega_1 = \text{sign}(\beta_1 - \beta_2/2)$ *and* $\omega_2 = \text{sign}(\beta_2 + \beta_1/2)$*, formula* (2.1) *can be rewritten as*

$$\mathrm{H}^* = (\omega_1\omega_2)\mathrm{H} + \pi\left(1 - \frac{1}{2}\omega_1\omega_2 - \frac{1}{2}\omega_2\right). \tag{2.2}$$

We then give an example to illustrate the effect of the improved definition of hue. We show the hue values of different colors by using the formulation of H^* in Fig. 2. We see from the figure that the hue values are in between $[0,2\pi]$, and different colors correspond to different unique hue values. Then it can be used as an effective color feature to distinguish different colors. We remark that the hue value has nothing to do with the saturation or the brightness of the color pixel. As we can see in Fig. 2 that the saturation of the chromatogram decreases vertically, however, the hue values are the same vertically.

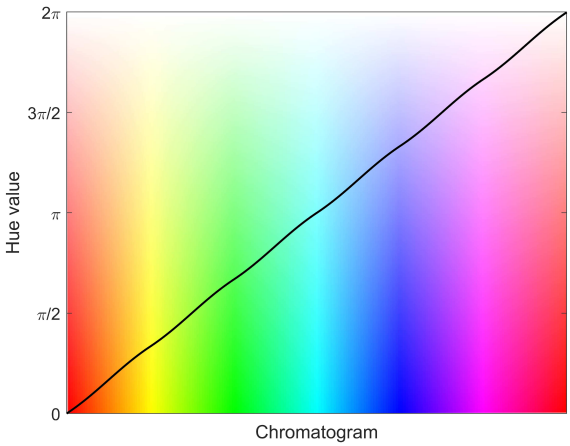

Figure 2: The hue values of the chromatogram.

3 Total variations for hue, saturation, and value

3.1 The formulation

Recall that Ω is a bounded and convex domain, $\partial_x u_k$ (or $\partial_y u_k$) is the partial derivative of u_k with respect to x (or y). We define the total variation for hue as follows:

$$\mathrm{HTV}(\mathbf{u}) := \int_\Omega \sqrt{\big(\partial_x \mathrm{H}^*(x,y)\big)^2 + \big(\partial_y \mathrm{H}^*(x,y)\big)^2}\, dxdy.$$

According to the definition of H^* given in (2.2), we can easily deduce the hue gradient as follows:

$$\partial_x \mathrm{H}^*(x,y) = (\omega_1\omega_2)\partial_x \mathrm{H}(x,y), \quad \partial_y \mathrm{H}^*(x,y) = (\omega_1\omega_2)\partial_y \mathrm{H}(x,y).$$

Noting that $\omega_1\omega_2$ can only be 1 or -1. Therefore,

$$\mathrm{HTV}(\mathbf{u}) = \int_\Omega \sqrt{\big(\partial_x \mathrm{H}(x,y)\big)^2 + \big(\partial_y \mathrm{H}(x,y)\big)^2}\, dxdy. \tag{3.1}$$

As introduced in [21], total variations for saturation, and value are given as follows based the conception of saturation/value gradient:

$$\mathrm{STV}(\mathbf{u}) = \int_\Omega \sqrt{|\partial_x \mathbf{u}(x,y)|_s^2 + |\partial_y \mathbf{u}(x,y)|_s^2}\, dxdy, \tag{3.2}$$

$$\mathrm{VTV}(\mathbf{u}) = \int_\Omega \sqrt{|\partial_x \mathbf{u}(x,y)|_v^2 + |\partial_y \mathbf{u}(x,y)|_v^2}\, dxdy, \tag{3.3}$$

where

$$\partial_x \mathbf{u}(x,y) = \begin{bmatrix} \partial_x u_r(x,y) \\ \partial_x u_g(x,y) \\ \partial_x u_b(x,y) \end{bmatrix}, \qquad \partial_y \mathbf{u}(x,y) = \begin{bmatrix} \partial_y u_r(x,y) \\ \partial_y u_g(x,y) \\ \partial_y u_b(x,y) \end{bmatrix},$$

$$|\partial_x \mathbf{u}(x,y)|_s = \|\mathbf{C}\partial_x \mathbf{u}(x,y)\|_2, \quad |\partial_y \mathbf{u}(x,y)|_s = \|\mathbf{C}\partial_y \mathbf{u}(x,y)\|_2,$$

$$|\partial_x \mathbf{u}(x,y)|_v = \frac{1}{\sqrt{3}}|\partial_x u_r(x,y) + \partial_x u_g(x,y) + \partial_x u_b(x,y)|,$$

$$|\partial_y \mathbf{u}(x,y)|_v = \frac{1}{\sqrt{3}}|\partial_y u_r(x,y) + \partial_y u_g(x,y) + \partial_y u_b(x,y)|.$$

We then define hue-saturation-value total variation (HSV-TV) by combining the total variations for hue (3.1), saturation (3.2) and value (3.3) as follows:

$$\begin{aligned}\mathrm{HSV\text{-}TV}(\mathbf{u}) := \int_\Omega &\sqrt{\big(\partial_x \mathrm{H}(x,y)\big)^2 + \big(\partial_y \mathrm{H}(x,y)\big)^2} + \alpha_1 \sqrt{|\partial_x \mathbf{u}(x,y)|_s^2 + |\partial_y \mathbf{u}(x,y)|_s^2} \\ &+ \alpha_2 \sqrt{|\partial_x \mathbf{u}(x,y)|_v^2 + |\partial_y \mathbf{u}(x,y)|_v^2}\, dxdy,\end{aligned} \tag{3.4}$$

where α_1 and α_2 are positive parameters given as the weights of the hue, saturation, and value components.

3.2 The dual formulation and properties of hue-saturation-value total variation

In this subsection, we study the dual formulation of HSV-TV, and we present several geometric properties of HSV-TV, including lower semi-continuity, compactness, etc. Before

further discussion, we recall the definition of the space of bounded variation functions ($\mathbb{BV}(\Omega)$).

Definition 3.1. *Suppose Ω is a bounded open subset of R^{2m} with a positive integer m. Let $\mathbb{B}^m$ denote the closed united ball in $\mathbb{R}^m$ and $\mathcal{K}^m=\mathcal{C}^1(\Omega,\mathbb{B}^{2m})$ be the set of continuously differentiable and bounded functions from the compact support in Ω to $\mathbb{B}^{2m}$. We define $\mathbb{BV}(\Omega)$ as follows:*

$$\mathbb{BV}(\Omega)=\left\{u\in L^1(\Omega);\int_\Omega |Du|=\sup_{\xi\in\mathcal{K}^m}\left\{\int_\Omega u\mathrm{div}\xi dx\right\}<\infty\right\},$$

where Du is called the distributional gradient of u.

We then give the dual formulation of HSV-TV in Definition 3.2. We also discuss the relationship between the dual formulation and the derivative-based definition (3.4) of HSV-TV in Proposition 3.1.

Definition 3.2 (Dual Formulation of HSV-TV)**.** *Assume that $u_r,u_g,u_b\in L^1(\Omega)$, then*

$$\begin{aligned}&\text{HSV-TV}_{dual}(\mathbf{u})\\ =&\sup_{\substack{\boldsymbol{\xi_1}\in\mathcal{K}^1,\\ (\boldsymbol{\xi_2},\boldsymbol{\xi_3})\in\mathcal{K}^2,\boldsymbol{\xi_4}\in\mathcal{K}^1}}\left\{\int_\Omega \mathrm{H}(\mathbf{u})\mathrm{div}(\boldsymbol{\xi_1})+\frac{\alpha_1}{\sqrt{2}}(u_g-u_b)\mathrm{div}(\boldsymbol{\xi_2})\right.\\ &\left.+\frac{\alpha_1}{\sqrt{6}}(2u_r-u_g-u_b)\mathrm{div}(\boldsymbol{\xi_3})+\frac{\alpha_2}{\sqrt{3}}(u_r+u_b+u_g)\mathrm{div}(\boldsymbol{\xi_4})dxdy\right\}.\end{aligned}\tag{3.5}$$

Proposition 3.1. *If $\mathbf{u}(x,y)$ is differential, then* $\text{HSV-TV}_{dual}(\mathbf{u})=\text{HSV-TV}(\mathbf{u})$.

Proof. If $\mathbf{u}(x,y)$ is differential, we can easily derive the following result by using [21, Proposition 3.1]:

$$\begin{aligned}&\int_\Omega \alpha_1\sqrt{|\partial_x\mathbf{u}(x,y)|_s^2+|\partial_y\mathbf{u}(x,y)|_s^2}+\alpha_2\sqrt{|\partial_x\mathbf{u}(x,y)|_v^2+|\partial_y\mathbf{u}(x,y)|_v^2}dxdy\\ =&\sup_{(\boldsymbol{\xi_2},\boldsymbol{\xi_3})\in\mathcal{K}^2,\boldsymbol{\xi_4}\in\mathcal{K}^1}\left\{\int_\Omega \frac{\alpha_1}{\sqrt{2}}(u_g-u_b)\mathrm{div}(\boldsymbol{\xi_2})+\frac{\alpha_1}{\sqrt{6}}(2u_r-u_g-u_b)\mathrm{div}(\boldsymbol{\xi_3})\right.\\ &\left.+\frac{\alpha_2}{\sqrt{3}}(u_r+u_b+u_g)\mathrm{div}(\boldsymbol{\xi_4})dxdy\right\}.\end{aligned}\tag{3.6}$$

Noting the definition of $\mathrm{HTV}(\mathbf{u})$ in (3.1), we can deduce that

$$\int_\Omega\sqrt{\left(\partial_x\mathrm{H}(x,y)\right)^2+\left(\partial_y\mathrm{H}(x,y)\right)^2}=\sup_{\boldsymbol{\xi_1}\in\mathcal{K}^1}\left\{\int_\Omega \mathrm{H}(\mathbf{u})\mathrm{div}(\boldsymbol{\xi_1})dxdy\right\}=\mathrm{HTV}(\mathbf{u}).\tag{3.7}$$

Eqs. (3.6) and (3.7) leads to (3.5). □

In order to show the lower semi-continuity of HSV-TV, we first give a lemma about the hue function $\mathrm{H}(\mathbf{u})$.

Lemma 3.1. *Assume that $u_r,u_g,u_b\in\mathbb{BV}(\Omega)$, and there exists $\epsilon_0>0$ such that $\|\mathbf{C_2u}\|>\epsilon_0$ in Ω, then $\mathrm{H}(x,y)\in\mathbb{BV}(\Omega)$.*

Proof. As defined in Definition 3.1, we need to prove that $\mathrm{H}(x,y)\in L^1(\Omega)$ and $\int_\Omega|D\mathrm{H}|<\infty$. As $\mathrm{H}(x,y)\subseteq[0,\pi/2]$ and Ω is bounded, we have

$$\int_\Omega \mathrm{H}(x,y)dxdy\leq\frac{\pi}{2}|\Omega|<\infty,$$

which means $\mathrm{H}(x,y)\in L^1(\Omega)$. We then prove that $\int_\Omega|D\mathrm{H}|<\infty$. Notice that $\|\mathbf{C_2u}\|>\epsilon_0$, therefore

$$\int_\Omega|D\mathrm{H}|=\int_\Omega\left|D\tan^{-1}\left(\frac{\|\mathbf{C_1u}\|}{\|\mathbf{C_2u}\|}\right)\right|\leq\int_\Omega\left|D\left(\frac{\|\mathbf{C_1u}\|}{\|\mathbf{C_2u}\|}\right)\right|\leq\frac{1}{\epsilon_0}\int_\Omega\big|D\|\mathbf{C_1u}\|\big|,$$

which means that $\int_\Omega|D\mathrm{H}|$ can be controlled by $\int_\Omega|D\|\mathbf{C_1u}\||$. Recall that $\|\mathbf{C_1u}\|=|u_g-u_b|/\sqrt{2}$, and $u_r,u_g,u_b\in\mathbb{BV}(\Omega)$, then the linear combination $(u_g-u_b)/\sqrt{2}\in\mathbb{BV}(\Omega)$, which gives

$$\int_\Omega\big|D\|\mathbf{C_1u}\|\big|<\infty.$$

Therefore, we can get that

$$\int_\Omega|D\mathrm{H}|<\infty. \tag{3.8}$$

The proof is complete. □

Proposition 3.2 (Lower Semi-Continuity)**.** *Let $\mathbf{u}^n=(u_r^n,u_g^n,u_b^n)^\top,\mathbf{u}=(u_r,u_g,u_b)^\top$. Assume that $u_r^n,u_g^n,u_b^n\in\mathbb{BV}(\Omega)$, and $u_r^n\to u_r,u_g^n\to u_g,u_b^n\to u_b$ in $L^1(\Omega)$, then*

$$\liminf_{n\to\infty}\mathrm{HSV\text{-}TV}(\mathbf{u}^n)\geq\mathrm{HSV\text{-}TV}(\mathbf{u}).$$

Proof. The lower semi-continuity of SV-TV has already given in [21], we only need to prove that

$$\liminf_{n\to\infty}\mathrm{HTV}(\mathbf{u}^n)\geq\mathrm{HTV}(\mathbf{u}).$$

Recall the definition of $\mathrm{HTV}(\mathbf{u})$, which can be written as the supremum of the following operator:

$$L:\mathbf{u}\ \mapsto\int_\Omega\mathrm{H}(\mathbf{u})\mathrm{div}(\boldsymbol{\xi})\,dxdy,$$

where $\boldsymbol{\xi}(x,y)\in\mathcal{K}^1$. As calculated in the appendix,

$$\|\mathbf{C_1u}\|=\frac{1}{\sqrt{2}}|u_g-u_b|,\quad\|\mathbf{C_2u}\|=\frac{1}{\sqrt{6}}|2u_r-u_g-u_b|.$$

Noting that $u_i^n\overset{L^1(\Omega)}{\longrightarrow}u_i,i=r,g,b$, we can easily deduce that

$$\big\|\mathbf{C_1u}^n\big\|\overset{L^1(\Omega)}{\longrightarrow}\|\mathbf{C_1u}\|,\quad\big\|\mathbf{C_2u}^n\big\|\overset{L^1(\Omega)}{\longrightarrow}\|\mathbf{C_2u}\|.$$

Therefore, we have $\mathrm{H}(\mathbf{u}^n) \xrightarrow{L^1(\Omega)} \mathrm{H}(\mathbf{u})$. Noting the linearity of L, we can deduce that

$$L\mathbf{u}^n \ \to \ L\mathbf{u}.$$

It follows that

$$L\mathbf{u} = \lim L\mathbf{u}^n = \liminf L\mathbf{u}^n \leq \liminf \left(\sup_{\xi \in \mathcal{K}^1} L\mathbf{u}^n \right) = \liminf \mathrm{HTV}(\mathbf{u}^n).$$

Then we can deduce the lower semi-continuity of HTV by taking the supremum,

$$\mathrm{HTV}(\mathbf{u}) \leq \liminf \mathrm{HTV}(\mathbf{u}^n).$$

Combine with the lower semi-continuity of SV-TV which is given in [21], we finally get

$$\text{HSV-TV}(\mathbf{u}) \leq \liminf \text{HSV-TV}(\mathbf{u}^n).$$

The proof is complete. □

Proposition 3.3 (Approximation). *For any* $\mathbf{u} = (u_r, u_g, u_b)^\top$ *with* $u_r, u_g, u_b \in BV(\Omega)$, *there exists a sequence* $\{\mathbf{u}^n = (u_r^n, u_g^n, u_b^n)^\top\}$ *with* $\{u_r^n\}, \{u_g^n\}, \{u_b^n\} \subset C^\infty(\Omega) \cap W^{1,1}(\Omega)$ *such that*

$$\begin{aligned}
&\lim_{n\to\infty} \int_\Omega |u_r^n - u_r| dxdy = 0, \\
&\lim_{n\to\infty} \int_\Omega |u_g^n - u_g| dxdy = 0, \\
&\lim_{n\to\infty} \int_\Omega |u_b^n - u_b| dxdy = 0, \\
&\lim_{n\to\infty} \text{HSV-TV}(\mathbf{u}^n) = \text{HSV-TV}(\mathbf{u}).
\end{aligned}$$

Proof. As is shown in [6], we can find three sequences $\{u_r^\epsilon\}, \{u_g^\epsilon\}, \{u_b^\epsilon\} \in C^\infty(\Omega) \cap W^{1,1}(\Omega)$ such that

$$\begin{aligned}
\int_\Omega |u_r^\epsilon - u_r| dxdy \ &\to \ 0, \\
\int_\Omega |u_g^\epsilon - u_g| dxdy \ &\to \ 0, \\
\int_\Omega |u_b^\epsilon - u_b| dxdy \ &\to \ 0
\end{aligned}$$

as $\epsilon \to 0$. Recall that [21] gives

$$\lim_{\epsilon\to 0}\text{SV-TV}(\mathbf{u}^\epsilon)=\text{SV-TV}(\mathbf{u}), \tag{3.9}$$

we then need to prove that

$$\lim_{\epsilon\to 0}\text{HTV}(\mathbf{u}^\epsilon)=\text{HTV}(\mathbf{u}).$$

Let L be the same definition as in the previous proof, then for fixed $\boldsymbol{\xi}\in\mathcal{K}^1$,

$$L\mathbf{u}=\lim_{\epsilon\to 0}L\mathbf{u}^\epsilon.$$

Therefore,

$$\lim_{\epsilon\to 0}L\mathbf{u}^\epsilon\le\text{HTV}(\mathbf{u}).$$

According to the above equation, we can find $\epsilon_0>0$ such that if $\epsilon<\epsilon_0$,

$$L\mathbf{u}^\epsilon\le\text{HTV}(\mathbf{u}).$$

Then for $\epsilon<\epsilon_0$,

$$\text{HTV}(\mathbf{u}^\epsilon)\le\text{HTV}(\mathbf{u}).$$

Noting the lower semi-continuity of HTV, we have

$$\text{HTV}(\mathbf{u})\le\liminf_{\epsilon\to 0}\text{HTV}(\mathbf{u}^\epsilon)\le\limsup_{\epsilon\to 0}\text{HTV}(\mathbf{u}^\epsilon)\le\text{HTV}(\mathbf{u}). \tag{3.10}$$

Combine (3.9) with (3.10), we derive the following result:

$$\lim_{n\to\infty}\text{HSV-TV}(\mathbf{u}^n)=\text{HSV-TV}(\mathbf{u}).$$

The proof is complete. □

Proposition 3.4 (Compactness)**.** *Assume* $\{\text{HSV-TV}(\mathbf{u}^n)+\sum_{i=r,g,b}\|u_i^n\|_{L^1}\}$ *is uniformly bounded, then there exist a subsequence (still noting as* $\{\mathbf{u}^n=(u_r^n,u_g^n,u_b^n)\}$*) and* $u_r,u_g,u_b\in BV(\Omega)$ *such that*

$$u_r^n\ \to\ u_r,\quad u_g^n\ \to\ u_g,\quad u_b^n\ \to\ u_b\quad in\ \ L^1(\Omega).$$

Proof. Set

$$v_1^n=\frac{u_g^n-u_b^n}{\sqrt{2}},\quad v_2^n=\frac{2u_r^n-u_g^n-u_b^n}{\sqrt{6}},\quad v_3^n=\frac{u_r^n+u_g^n+u_b^n}{\sqrt{3}}.$$

By the dual form of $\text{HSV-TV}(\mathbf{u}^n)$ given in (3.5), we have

$$\begin{aligned}\text{HSV-TV}(\mathbf{u}^n)=\sup_{\substack{\boldsymbol{\xi_1}\in\mathcal{K}^1,(\boldsymbol{\xi_2},\boldsymbol{\xi_3})\in\mathcal{K}^2,\\ \boldsymbol{\xi_4}\in\mathcal{K}^1}}\Bigg\{\int_\Omega\tan^{-1}\left(\frac{v_1^n}{v_2^n}\right)\text{div}(\boldsymbol{\xi_1})+\alpha_1 v_1^n\text{div}(\boldsymbol{\xi_2})\\ +\alpha_1 v_2^n\text{div}(\boldsymbol{\xi_3})+\alpha_2 v_3^n\text{div}(\boldsymbol{\xi_4})dxdy\Bigg\}.\end{aligned}$$

By using the boundedness of HSV-TV($\mathbf{u}^n$) and noting that v_i^n ($i=1,2,3$) is a linear combination of u_r^n, u_g^n, u_b^n, we can easily deduce that $\{v_1^n\}, \{v_2^n\}, \{v_3^n\}$ are uniformly bounded in $\mathbb{BV}(\Omega)$. Noting the compactness of $\mathbb{BV}(\Omega)$, there exist three subsequences (still noting as $\{v_1^n\}, \{v_2^n\}, \{v_3^n\}$) and $v_1, v_2, v_3 \in \mathbb{BV}(\Omega)$ such that

$$v_1^n \ \to\ v_1, \quad v_2^n \ \to\ v_2, \quad v_3^n \ \to v_3 \quad \text{in } L^1(\Omega).$$

By the given relationship between u_r^n, u_g^n, u_b^n and v_1^n, v_2^n, v_3^n above, it is easy to deduce that

$$u_r^n = \frac{\sqrt{6}v_2^n + \sqrt{3}v_3^n}{3}, \quad u_g^n = \frac{3\sqrt{2}v_1^n - \sqrt{6}v_2^n + 2\sqrt{3}v_3^n}{6}, \quad u_b^n = \frac{-3\sqrt{2}v_1^n - \sqrt{6}v_2^n + 2\sqrt{3}v_3^n}{6},$$

which means u_r^n, u_g^n, u_b^n are the linear combinations of v_1^n, v_2^n, v_3^n. We derive that there exist a subsequence (still noting as $\{\mathbf{u}^n = (u_r^n, u_g^n, u_b^n)\}$) and $u_r, u_g, u_b \in \mathbb{BV}(\Omega)$ such that

$$u_r^n \to u_r, \quad u_g^n \to u_g, \quad u_b^n \to u_b \quad \text{in } L^1(\Omega).$$

This completes the proof. □

3.3 Total variation model for color image restoration

In this subsection, we study the following hue-saturation-value total variation model for color image restoration:

$$\min_{u_r, u_g, u_b \in \mathbb{BV}(\Omega)} \left\{ \mathbf{E}(\mathbf{u}) = \text{HSV-TV}(\mathbf{u}) + \frac{\lambda}{2} \int_\Omega |(\mathrm{K} \star \mathbf{u})(x,y) - \mathbf{z}(x,y)|^2 dxdy \right\}. \tag{3.11}$$

Here, Ω is a bounded open subset of R^2. The first term is the proposed hue-saturation-value total variation which is used for color image regularization. The second term is the data-fitting term, where $\mathbf{z}(x,y)$ is the given noisy image, $\lambda > 0$ is a positive parameter which is used to balance these two terms, and K is a given blurring operator, $\star$ is the convolution operation. Noting that HSV-TV($\mathbf{u}$) is nonconvex, we conclude the existence of the minimizer of the proposed problem (3.11) in the following theorem.

Theorem 3.1. *The minimization problem* (3.11) *has at least one solution.*

Proof. First, if we set $\mathbf{u}(x,y)$ to be constant, then HSV($\mathbf{u}$) is finite, which implies that the infimum of $\mathbf{E}(\mathbf{u})$ is finite, i.e. the proposed minimization problem is well defined. Assume that $\mathbf{u}^{(n)} = [u_r^{(n)}\ u_g^{(n)}\ u_b^{(n)}]^\top$ is a minimizing sequence of (3.11), then there exists a constant $M > 0$ such that

$$\text{HSV-TV}(\mathbf{u}^{(n)}) \le M.$$

Notice that the data-fitting term is a coercive functional with respect to $\mathbf{u}$, we get that $\|u_i^{(n)}\|_{L^2}$ is uniformly bounded for $i = r, g, b$. By using Holder inequality, we have

$$\left\|u_i^{(n)}\right\|_{L^1} \le \left\|u_i^{(n)}\right\|_{L^2} \|1\|_{L^2}.$$

Combine with the boundedness of Ω, we can deduce that $\|u_i^{(n)}\|_{L^1}$ is uniformly bounded for $i=r,g,b$. Then $\{\text{HSV-TV}(\mathbf{u}^{(n)})+\sum_{i=r,g,b}\|u_i^{(n)}\|_{L^1}\}$ is uniformly bounded. By using Proposition 3.4, up to a subsequence (also denoted by $u_r^{(n)},u_g^{(n)},u_b^{(n)}$), there exists $\tilde{\mathbf{u}}(x,y)=[\tilde{u_r}(x,y),\tilde{u_g}(x,y),\tilde{u_b}(x,y)]^\top$ $(\tilde{u_r},\tilde{u_g},\tilde{u_b}\in\mathbb{BV}(\Omega))$ satisfying that

$$\begin{aligned}
u_r^{(n)}(x,y) &\xrightarrow{L^1(\Omega)} \tilde{u_r}(x,y), \quad u_r^{(n)}(x,y) \to \tilde{u_r}(x,y) \quad \text{a.e.} \quad (xy)\in\Omega,\\
u_g^{(n)}(x,y) &\xrightarrow{L^1(\Omega)} \tilde{u_g}(x,y), \quad u_g^{(n)}(x,y) \to \tilde{u_g}(x,y) \quad \text{a.e.} \quad (x,y)\in\Omega,\\
u_b^{(n)}(x,y) &\xrightarrow{L^1(\Omega)} \tilde{u_b}(x,y), \quad u_b^{(n)}(x,y) \to \tilde{u_b}(x,y) \quad \text{a.e.} \quad (x,y)\in\Omega.
\end{aligned}$$

Noting the lower semi-continuity given in Proposition 3.2, we have

$$\liminf \text{HSV-TV}(\mathbf{u}^{(n)}) \geq \text{HSV-TV}(\tilde{\mathbf{u}}). \tag{3.12}$$

Meanwhile, the following convergence results hold:

$$\begin{aligned}
\big((\mathrm{K}\star u_r^{(n)})(x,y)-\mathbf{z}(x,y)\big)^2 &\to \big((\mathrm{K}\star \tilde{u_r})(x,y)-\mathbf{z}(x,y)\big)^2 \quad \text{a.e.} \quad (x,y)\in\Omega,\\
\big((\mathrm{K}\star u_g^{(n)})(x,y)-\mathbf{z}(x,y)\big)^2 &\to \big((\mathrm{K}\star \tilde{u_g})(x,y)-\mathbf{z}(x,y)\big)^2 \quad \text{a.e.} \quad (x,y)\in\Omega,\\
\big((\mathrm{K}\star u_b^{(n)})(x,y)-\mathbf{z}(x,y)\big)^2 &\to \big((\mathrm{K}\star \tilde{u_b})(x,y)-\mathbf{z}(x,y)\big)^2 \quad \text{a.e.} \quad (x,y)\in\Omega.
\end{aligned}$$

By using Fatou's lemma, we have

$$\begin{aligned}
&\liminf \int_\Omega \big((\mathrm{K}\star u_r^{(n)})(x,y)-\mathbf{z}(x,y)\big)^2dxdy+\int_\Omega \big((\mathrm{K}\star u_g^{(n)})(x,y)-\mathbf{z}(x,y)\big)^2dxdy\\
&\quad+\int_\Omega \big((\mathrm{K}\star u_b^{(n)})(x,y)-\mathbf{z}(x,y)\big)^2dxdy\\
\geq &\int_\Omega \big((\mathrm{K}\star \tilde{u_r})(x,y)-\mathbf{z}(x,y)\big)^2dxdy+\int_\Omega \big((\mathrm{K}\star \tilde{u_g})(x,y)-\mathbf{z}(x,y)\big)^2dxdy\\
&\quad+\int_\Omega \big((\mathrm{K}\star \tilde{u_b})(x,y)-\mathbf{z}(x,y)\big)^2dxdy.
\end{aligned} \tag{3.13}$$

Combine with the lower semi-continuity and (3.13), we have

$$\begin{aligned}
&\liminf \text{HSV-TV}\left(\mathbf{u}^{(n)}\right)+\frac{\lambda}{2}\int_\Omega \left|\left(\mathrm{K}\star\mathbf{u}^{(n)}\right)(x,y)-\mathbf{z}(x,y)\right|^2dxdy\\
\geq &\,\text{HSV-TV}(\tilde{\mathbf{u}})+\frac{\lambda}{2}\int_\Omega |(\mathrm{K}\star\tilde{\mathbf{u}})(x,y)-\mathbf{z}(x,y)|^2dxdy.
\end{aligned} \tag{3.14}$$

It leads to the existence of the solution of (3.11). □

On the other hand, the Euler-Lagrange equation of the proposed HSV-TV model is given as

$$
\begin{aligned}
&-\nabla\cdot\left(\frac{\mathrm{H_r}\nabla \mathrm{H}}{\mathrm{HTV}(\mathbf{u})}+\alpha_1\frac{\nabla(2u_r-u_g-u_b)}{3\sqrt{|\partial_x\mathbf{u}|_s^2+|\partial_y\mathbf{u}|_s^2}}+\alpha_2\frac{\nabla(u_r+u_g+u_b)}{3\sqrt{|\partial_x\mathbf{u}|_v^2+|\partial_y\mathbf{u}|_v^2}}\right)\\
&\quad+\frac{\partial_x\mathrm{H}\partial_x\mathrm{H_r}}{\mathrm{HTV}(\mathbf{u})}+\frac{\partial_y\mathrm{H}\partial_y\mathrm{H_r}}{\mathrm{HTV}(\mathbf{u})}+\lambda(\mathrm{K}^*\star\mathrm{K}\star u_r-\mathrm{K}^*\star z_r)=0,\\
&-\nabla\cdot\left(\frac{\mathrm{H_g}\nabla \mathrm{H}}{\mathrm{HTV}(\mathbf{u})}+\alpha_1\frac{\nabla(2u_g-u_r-u_b)}{3\sqrt{|\partial_x\mathbf{u}|_s^2+|\partial_y\mathbf{u}|_s^2}}+\alpha_2\frac{\nabla(u_r+u_g+u_b)}{3\sqrt{|\partial_x\mathbf{u}|_v^2+|\partial_y\mathbf{u}|_v^2}}\right)\\
&\quad+\frac{\partial_x\mathrm{H}\partial_x\mathrm{H_g}}{\mathrm{HTV}(\mathbf{u})}+\frac{\partial_y\mathrm{H}\partial_y\mathrm{H_g}}{\mathrm{HTV}(\mathbf{u})}+\lambda(\mathrm{K}^*\star\mathrm{K}\star u_g-\mathrm{K}^*\star z_g)=0,\\
&-\nabla\cdot\left(\frac{\mathrm{H_b}\nabla \mathrm{H}}{\mathrm{HTV}(\mathbf{u})}+\alpha_1\frac{\nabla(2u_b-u_r-u_b)}{3\sqrt{|\partial_x\mathbf{u}|_s^2+|\partial_y\mathbf{u}|_s^2}}+\alpha_2\frac{\nabla(u_r+u_g+u_b)}{3\sqrt{|\partial_x\mathbf{u}|_v^2+|\partial_y\mathbf{u}|_v^2}}\right)\\
&\quad+\frac{\partial_x\mathrm{H}\partial_x\mathrm{H_n}}{\mathrm{HTV}(\mathbf{u})}+\frac{\partial_y\mathrm{H}\partial_y\mathrm{H_b}}{\mathrm{HTV}(\mathbf{u})}+\lambda(\mathrm{K}^*\star\mathrm{K}\star u_b-\mathrm{K}^*\star z_b)=0,
\end{aligned}
$$

where K^* is the conjugate transpose of K, and

$$
\mathrm{H_r}=\beta_1\beta_2\frac{u_b-u_g}{\sqrt{3}||\mathbf{Cu}||^2},\quad \mathrm{H_g}=\beta_1\beta_2\frac{u_r-u_b}{\sqrt{3}||\mathbf{Cu}||^2},\quad \mathrm{H_b}=\beta_1\beta_2\frac{u_g-u_r}{\sqrt{3}||\mathbf{Cu}||^2}. \tag{3.15}
$$

The detailed calculations are shown in Appendix A. We see from the above equations that HSV-TV takes the form of coupling channel-wise diffusion coefficients in the hue component, saturation component, and value component. Meanwhile, HSV-TV takes the form of three diffusion equations corresponding to three color channels, and each diffusion equation still involves three color channel variables. Because of deep coupling among three color channels in diffusion coefficients and equations, we expect that the color image restoration may be enhanced. In Section 5, numerical examples are given to demonstrate the effectiveness of the proposed model.

4 Numerical algorithm for HSV-TV model

4.1 Numerical algorithm

In this section, we make use of an alternating iterative algorithm to solve the proposed optimization problem (3.11). Let

$$
J(\mathbf{u})=\text{HSV-TV}(\mathbf{u}),
$$

we then solve (3.11) according to the following scheme.

Algorithm 1.

1: Initialization: Set $\mathbf{u}^0=\mathbf{z}$.

2: For fixed u_g^k,u_b^k, update u_r^{k+1} by solving

$$\min_{u_r}\left\{J\left(u_r,u_g^k,u_b^k\right)+\frac{\lambda}{2}\int_\Omega(\mathrm{K}\star u_r-z_r)^2dxdy\right\}. \tag{4.1}$$

3: For fixed u_r^{k+1},u_b^k, update u_g^{k+1} by solving

$$\min_{u_g}\left\{J\left(u_r^{k+1},u_g,u_b^k\right)+\frac{\lambda}{2}\int_\Omega(\mathrm{K}\star u_g-z_g)^2dxdy\right\}. \tag{4.2}$$

4: For fixed u_r^{k+1},u_g^{k+1}, update u_b^{k+1} by solving

$$\min_{u_b}\left\{J\left(u_r^{k+1},u_g^{k+1},u_b\right)+\frac{\lambda}{2}\int_\Omega(\mathrm{K}\star u_b-z_b)^2dxdy\right\}. \tag{4.3}$$

5: Stop the iteration until $\|u_r^{k+1}-u_r^k\|/\|u_r^k\|<\epsilon$ for fixed ϵ.

The Euler-Lagrange equations of (4.1)-(4.3) are given as follows:

$$\begin{aligned}
&0\in\partial J\left(u_r,u_g^k,u_b^k\right)+\lambda\mathrm{K}^*\star(\mathrm{K}\star u_r-z_r),\\
&0\in\partial J\left(u_r^{k+1},u_g,u_b^k\right)+\lambda\mathrm{K}^*\star(\mathrm{K}\star u_g-z_g),\\
&0\in\partial J\left(u_r^{k+1},u_g^{k+1},u_b\right)+\lambda\mathrm{K}^*\star(\mathrm{K}\star u_b-z_b),
\end{aligned}$$

where K^* is the conjugate transpose of K. Numerically, we consider the following implicit scheme of the evolution equations:

$$0\in\frac{u_r-u_r^k}{\tau}+\partial J\left(u_r,u_g^k,u_b^k\right)+\lambda\mathrm{K}^*\star(\mathrm{K}\star u_r-z_r), \tag{4.4}$$

$$0\in\frac{u_g-u_g^k}{\tau}+\partial J\left(u_r^{k+1},u_g,u_b^k\right)+\lambda\mathrm{K}^*\star(\mathrm{K}\star u_g-z_g), \tag{4.5}$$

$$0\in\frac{u_b-u_b^k}{\tau}+\partial J\left(u_r^{k+1},u_g^{k+1},u_b\right)+\lambda\mathrm{K}^*\star(\mathrm{K}\star u_b-z_b). \tag{4.6}$$

Let

$$\begin{aligned}
&J_r(u_r)=J\left(u_r,u_g^k,u_b^k\right), && h(u_r)=\frac{1}{2}\left((\mathrm{K}\star u_r)-z_r\right)^2,\\
&J_g(u_g)=J\left(u_r^{k+1},u_g,u_b^k\right), && h(u_g)=\frac{1}{2}\left((\mathrm{K}\star u_g)-z_g\right)^2,\\
&J_b(u_b)=J\left(u_r^{k+1},u_g^{k+1},u_b\right), && h(u_b)=\frac{1}{2}\left((\mathrm{K}\star u_b)-z_b\right)^2.
\end{aligned}$$

We then use the following evolution equations to solve (4.4)-(4.6):

$$u_r^{t+1}=u_r^t-\tau_t\Big(u_r^t-u_r^k+\tau\big(\partial J_r\big(u_r^t\big)+\lambda \mathrm{K}^*\star\big(\mathrm{K}\star u_r^t-z_r\big)\big)\Big),$$
$$u_g^{t+1}=u_g^t-\tau_t\Big(u_g^t-u_g^k+\tau\big(\partial J_g\big(u_g^t\big)+\lambda \mathrm{K}^*\star\big(\mathrm{K}\star u_g^t-z_g\big)\big)\Big),$$
$$u_b^{t+1}=u_b^t-\tau_t\Big(u_b^t-u_b^k+\tau\big(\partial J_b\big(u_b^t\big)+\lambda \mathrm{K}^*\star\big(\mathrm{K}\star u_b^t-z_b\big)\big)\Big).$$

Meanwhile, we remark that solving Eqs. (4.4)-(4.6) are equivalent to deal with the following minimizing problems:

$$u_r^{k+1}=\underset{u_r}{\operatorname{argmin}}\Big\{F_r\big(u_r,u_r^k\big)=\int_\Omega\frac{u_r^2}{2}dxdy-\int_\Omega u_r^k u_r dxdy + \tau\left(J_r(u_r)+\lambda\int_\Omega h(u_r)dxdy\right)\Big\}, \tag{4.7}$$

$$u_g^{k+1}=\underset{u_g}{\operatorname{argmin}}\Big\{F_r\big(u_g,u_g^k\big)=\int_\Omega\frac{u_g^2}{2}dxdy-\int_\Omega u_g^k u_g dxdy + \tau\left(J_r(u_g)+\lambda\int_\Omega h(u_g)dxdy\right)\Big\}, \tag{4.8}$$

$$u_b^{k+1}=\underset{u_b}{\operatorname{argmin}}\Big\{F_r\big(u_b,u_b^k\big)=\int_\Omega\frac{u_b^2}{2}dxdy-\int_\Omega u_b^k u_b dxdy + \tau\left(J_r(u_b)+\lambda\int_\Omega h(u_b)dxdy\right)\Big\}. \tag{4.9}$$

4.2 Convergence analysis

In this section, we study the convergence of the proposed algorithm. We first give two propositions about the energy functionals J_r, J_g and J_b.

Proposition 4.1. *There exists* $u_r^{k+1},u_g^{k+1},u_b^{k+1}\in\mathbb{BV}(\Omega)$ *satisfying* (4.7)-(4.9). *Moreover, we have*

$$J_r\big(u_r^k\big)\le J_r\big(u_r^0\big)+\lambda\int_\Omega h\big(u_r^0\big)dxdy, \tag{4.10}$$
$$J_r\big(u_g^k\big)\le J_g\big(u_g^0\big)+\lambda\int_\Omega h\big(u_g^0\big)dxdy, \tag{4.11}$$
$$J_r\big(u_b^k\big)\le J_b\big(u_b^0\big)+\lambda\int_\Omega h\big(u_b^0\big)dxdy. \tag{4.12}$$

Proof. We set

$$h_k(u_r)=\tau\lambda h(u_r)+\frac{u_r^2}{2}-u_r^k u_r.$$

Then we have

$$F_r(u_r,u_r^k)=\tau J_r(u_r)+\int_\Omega h_k dxdy.$$

By using similar arguments as in the proof of Theorem 3.1, we can easily derive the existence of u_r^{k+1},u_g^{k+1}, and u_b^{k+1}. We then prove (4.10). By using formula (4.7), we have

$$F_r(u_r^{k+1},u_r^k)\le F_r(u_r^k,u_r^k).$$

It reads

$$\tau\left(J_r(u_r^{k+1})-J_r(u_r^k)+\lambda\int_\Omega\big(h(u_r^{k+1})-h(u_r^k)\big)dxdy\right)+\frac{1}{2}\int_\Omega(u_r^{k+1}-u_r^k)^2dxdy\le 0.$$

Therefore, we have

$$J_r(u_r^{k+1})-J_r(u_r^k)+\lambda\int_\Omega\big(h(u_r^{k+1})-h(u_r^k)\big)dxdy\le 0.$$

We can get the following inequalities by using similar arguments:

$$\begin{aligned}
&J_r(u_r^k)-J_r(u_r^{k-1})+\lambda\int_\Omega\big(h(u_r^k)-h(u_r^{k-1})\big)dxdy\le 0,\\
&J_r(u_r^{k-1})-J_r(u_r^{k-2})+\lambda\int_\Omega\big(h(u_r^{k-1})-h(u_r^{k-2})\big)dxdy\le 0,\\
&\cdots\cdots\cdots\cdots\cdots\cdots\cdots\cdots\cdots\cdots\cdots\cdots\cdots\cdots\cdots\cdots\\
&J_r(u_r^1)-J_r(u_r^0)+\lambda\int_\Omega\big(h(u_r^1)-h(u_r^0)\big)dxdy\le 0.
\end{aligned}$$

By taking the summation of both sides, we get

$$J_r(u_r^k)-J_r(u_r^0)+\lambda\int_\Omega\big(h(u_r^k)-h(u_r^0)\big)dxdy\le 0.$$

Notice that $h(u_r)\ge 0$ always holds, we have

$$J_r(u_r^k)-J_r(u_r^0)-\lambda\int_\Omega h(u_r^0)dxdy\le 0,\quad i.e.\quad J_r(u_r^k)\le J_r(u_r^0)+\lambda\int_\Omega h(u_r^0)dxdy.$$

We can derive the other two inequalities (4.11) and (4.12) by using similar arguments. □

Proposition 4.2. *Assume that $u_r^k,u_g^k,u_b^k\in\mathbb{BV}(\Omega)$ satisfy*

$$u_r^k\xrightarrow{L^1(\Omega)}\tilde{u_r},\quad u_g^k\xrightarrow{L^1(\Omega)}\tilde{u_g},\quad u_b^k\xrightarrow{L^1(\Omega)}\tilde{u_b},$$

then

$$\liminf J_r(u_r^k)\ge J_r(\tilde{u_r}),\quad \liminf J_r(u_r^g)\ge J_r(\tilde{u_g}),\quad \liminf J_r(u_r^b)\ge J_r(\tilde{u_b}).$$

Proof. Recall that $J_r(u_r)=J(u_r,u_g^{k_0},u_b^{k_0})$, where the index k_0 is fixed. As

$$u_r^k \xrightarrow{L^1(\Omega)} \tilde{u_r}, \quad u_g^{k_0} \xrightarrow{L^1(\Omega)} u_g^{k_0}, \quad u_b^{k_0} \xrightarrow{L^1(\Omega)} u_b^{k_0}$$

naturally hold, we can easily deduce the following result by applying Proposition 3.2:

$$J_r(\tilde{u_r}) \leq \liminf J_r\left(u_r^k\right).$$

We can derive the other two inequalities by using similar arguments. □

Now we show the following convergence result of the proposed implicit scheme.

Theorem 4.1. *There exists $(\tilde{u_r},\tilde{u_g},\tilde{u_b})$ in $\mathbb{BV}(\Omega)$ satisfying that $u_r^k \to \tilde{u_r}, u_g^k \to \tilde{u_g}, u_b^k \to \tilde{u_b}$ (up to subsequences) for the $\mathbb{BV}(\Omega)$ weak* topology, where (u_r^k,u_g^k,u_b^k) are defined as in* (4.4)-(4.6)*, and $(\tilde{u_r},\tilde{u_g},\tilde{u_b})$ are the solutions of*

$$0\in\partial J_r(\tilde{u_r})+\lambda h^{'}(\tilde{u_r}), \quad 0\in\partial J_g(\tilde{u_g})+\lambda h^{'}(\tilde{u_g}), \quad 0\in\partial J_b(\tilde{u_b})+\lambda h^{'}(\tilde{u_b}).$$

Proof. As in the proof of Proposition 4.1, we have the similar inequalities

$$\begin{aligned}
&\frac{1}{2}\int_\Omega \left(u_r^{k+1}-u_r^k\right)^2 dxdy \leq \tau\left(J_r\left(u_r^k\right)-J_r\left(u_r^{k+1}\right)+\lambda\int_\Omega\left(h\left(u_r^k\right)-h\left(u_r^{k+1}\right)\right)dxdy\right),\\
&\frac{1}{2}\int_\Omega \left(u_r^{k}-u_r^{k-1}\right)^2 dxdy \leq \tau\left(J_r\left(u_r^{k-1}\right)-J_r\left(u_r^{k}\right)+\lambda\int_\Omega\left(h\left(u_r^{k-1}\right)-h\left(u_r^{k}\right)\right)dxdy\right),\\
&\cdots\cdots\cdots\cdots\cdots\cdots\cdots\cdots\cdots\cdots\cdots\cdots\cdots\cdots\cdots\cdots\cdots\cdots\cdots\cdots\cdots\cdots\\
&\frac{1}{2}\int_\Omega \left(u_r^{1}-u_r^{0}\right)^2 dxdy \leq \tau\left(J_r\left(u_r^{0}\right)-J_r\left(u_r^{1}\right)+\lambda\int_\Omega\left(h\left(u_r^{0}\right)-h\left(u_r^{1}\right)\right)dxdy\right).
\end{aligned}$$

By taking summation of both sides where $k<K$, we have

$$\begin{aligned}
\frac{1}{2}\sum_{k=0}^{K-1}\int_\Omega \left(u_r^{k+1}-u_r^k\right)^2 dxdy &\leq \tau\left(J_r\left(u_r^0\right)-J_r\left(u_r^K\right)+\lambda\int_\Omega\left(h\left(u_r^0\right)-h\left(u_r^K\right)\right)dxdy\right)\\
&\leq \tau\left(J_r\left(u_r^0\right)+\lambda\int_\Omega h\left(u_r^0\right)dxdy\right)<+\infty.
\end{aligned}$$

It implies that

$$u_r^{k+1}-u_r^k \xrightarrow{L^2(\Omega)} 0. \tag{4.13}$$

By using the estimation (4.10), and noting the boundedness of u_r, we know that there exists $\tilde{u_r}$ in $\mathbb{BV}(\Omega)$ such that up to a subsequence,

$$u_r^k \rightarrow \tilde{u_r} \quad \text{for } \mathbb{BV}(\Omega) \text{ weak* topology.}$$

Moreover,

$$u_r^k \xrightarrow{L^1(\Omega)} \tilde{u_r}. \tag{4.14}$$

By using formula (4.7), we have

$$0 \in \frac{u_r^{k+1}-u_r^k}{\tau} + \partial J_r\left(u_r^{k+1}\right) + \lambda h^{'}\left(u_r^{k+1}\right),$$

which means for $v_r \in L^2(\Omega)$,

$$J_r(v_r) \geq J_r\left(u_r^{k+1}\right) + \left\langle v_r - u_r^{k+1}, -\frac{u_r^{k+1}-u_r^k}{\tau} - \lambda h^{'}\left(u_r^{k+1}\right) \right\rangle_{L^2(\Omega)}.$$

Therefore, by using (4.14), and combining with Lebesgue's dominated convergence theorem, we derive that up to a subsequence

$$u_r^k \xrightarrow{L^2(\Omega)} \tilde{u_r}. \tag{4.15}$$

By using Proposition 4.2 and the convergence results (4.13) and (4.15), we derive

$$\begin{aligned} &\liminf J_r(u_r^{k+1}) \geq J_r(\tilde{u_r}), \\ &\left\langle v_r - u_r^{k+1}, -\frac{u_r^{k+1}-u_r^k}{\tau} - \lambda h^{'}\left(u_r^{k+1}\right) \right\rangle_{L^2(\Omega)} \rightarrow \left\langle v_r - \tilde{u_r}, -\lambda h^{'}(\tilde{u_r}) \right\rangle_{L^2(\Omega)}. \end{aligned}$$

Let $k \rightarrow +\infty$, we have

$$J_r(v_r) \geq J_r(\tilde{u_r}) + \left\langle v_r - \tilde{u_r}, -\lambda h^{'}(\tilde{u_r}) \right\rangle_{L^2(\Omega)}.$$

It implies

$$0 \in \partial J_r(\tilde{u_r}) + \lambda h^{'}(\tilde{u_r}).$$

We can derive the other two results by using similar arguments. □

5 Numerical experiments

To demonstrate the effectiveness of the proposed restoration model, we present the numerical results in this section. We compare the proposed HSV-TV model with C-TV [4], V-TV [30], GV-TV [28], and SV-TV [21] on several testing methods. The quality of the recovered images is measured by

- Peak signal-to-noise ratio (PSNR), an index to measure the ratio between the maximum possible power of a signal and the power of corrupting noise that affects the fidelity of its representation.
- Structural Similarity (SSIM) [35], an index to measure the similarity of two images, which has been proven to be consistent with human eye perception.

- S-CIELAB color metric [40], which includes a spatial processing step and is useful and efficient for measuring color reproduction errors of digital images.

In the following experiments, we report the best result in terms of the best PSNR value corresponding to the optimal regularization parameter in some ranges. In the proposed HSV-TV model, parameters α_1 and α_2 control STV and VTV respectively. Therefore, higher α_1 value leads to more saturation smoothing and higher α_2 value results in more value smoothing. For the proposed HSV-TV model, we set $\alpha_1 = 0.35, \alpha_2 = 0.15$ in all the experiments, and the range of λ is set as $[0.001, 0.004]$. For SV-TV model, we set $\alpha = 0.15$ and $\beta = 0.1$ in all the experiments, and the range of λ is set as $[0.002, 0.008]$. For C-TV model, we set $\beta = 0.1$ in all the experiments, and the range of λ is set as $[0.001, 0.003]$. For V-TV model and GV-TV model, the range of λ is also set as $[0.001, 0.003]$. For the stopping criteria, we break the iterations when the relative error of the successive iterates is less than or equal to 1×10^{-6} for all the testing methods. The proposed main algorithm is implemented in MATLAB. All the computations are performed on a PC with an AMD Ryzen 7 5800H 3.20 GHz CPU.

We make use of 80 images taken from the Berkeley Segmentation Database5 [24] to test the proposed HSV-TV model for color image restoration with respect to different levels of degradations. Several ground-truth images are shown in Fig. 3.

Figure 3: Ground truth images.

5.1 Image denoising I: Low noise level

In the first experiment, we artificially add Gaussian noise of standard deviation 0.1 to degrade the ground-truth color images in each channel, and compute the PSNR, SSIM values and S-CIELAB error pixel numbers for each restored result by comparing it with the ground-truth image. By choosing the optimal value of the regularization parameter in terms of PSNR value for each testing method, we obtained the optimal restored result and the corresponding values of the measures.

As examples, we show several restored results in Figs. 4-7. We can clearly see from the output images that HSV-TV model and SV-TV model are more effective in handling color artifacts, see especially the color artifacts on the surface of the rock (Figs. 4, 5 and 7) and the grass (Fig. 6). Meanwhile, the proposed HSV-TV model is more effective in saturation retention compared with SV-TV model, see the high saturation parts of the restored results such as the red jacket (Figs. 4 and 5), the fur of the lion (Fig. 6) and the cat (Fig. 7).

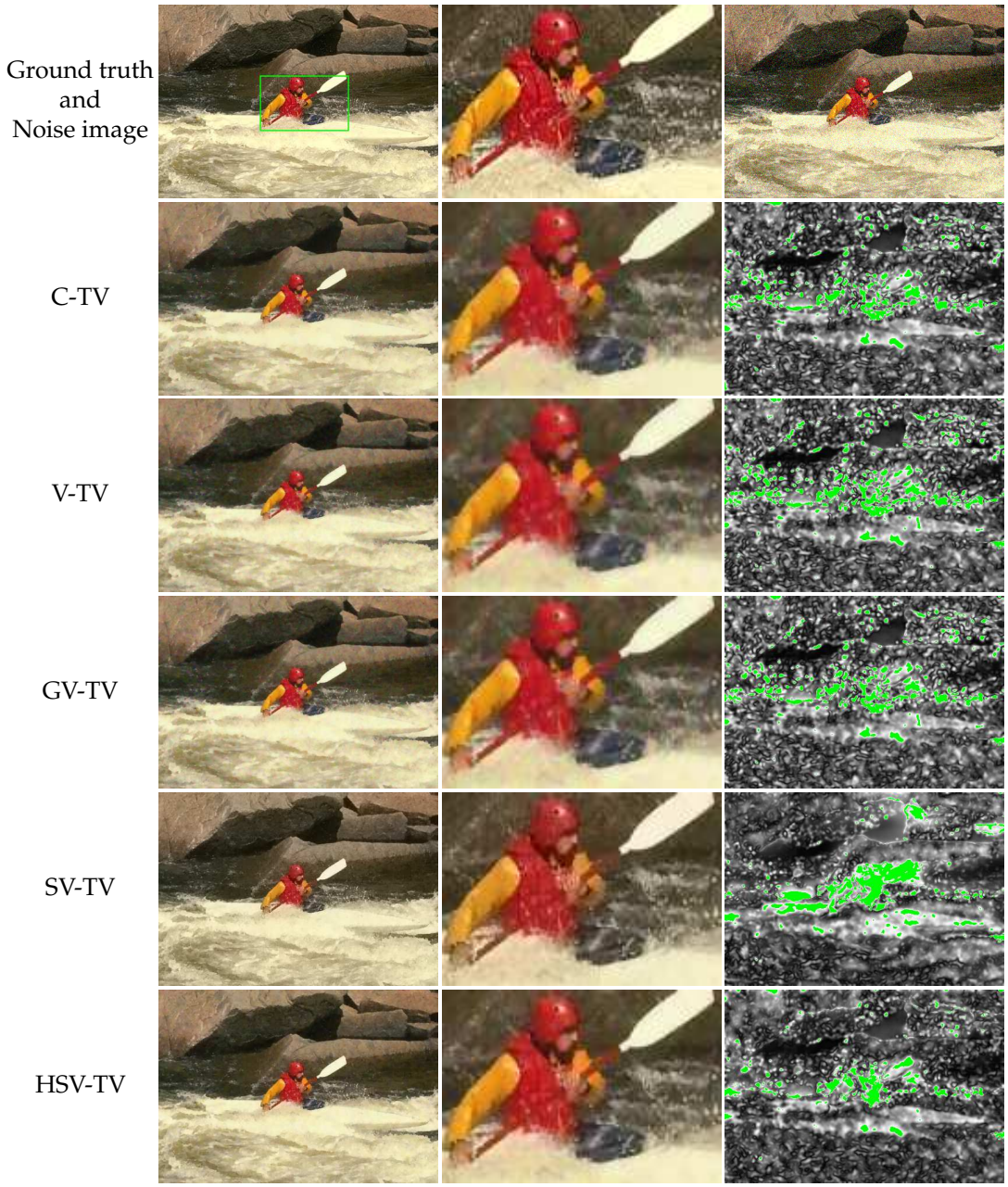

Figure 4: From left to right: The restored results of noisy level $\sigma = 0.1$, the corresponding zooming parts, and the spatial distribution of S-CIELAB error pixel (exceeding 5 units).

Furthermore, we display the spatial distributions of S-CIELAB color errors in the third column of each figure. The pixel with the error of 5 units or higher is marked by green. We find from the resulting spatial distributions that the color error between the restored

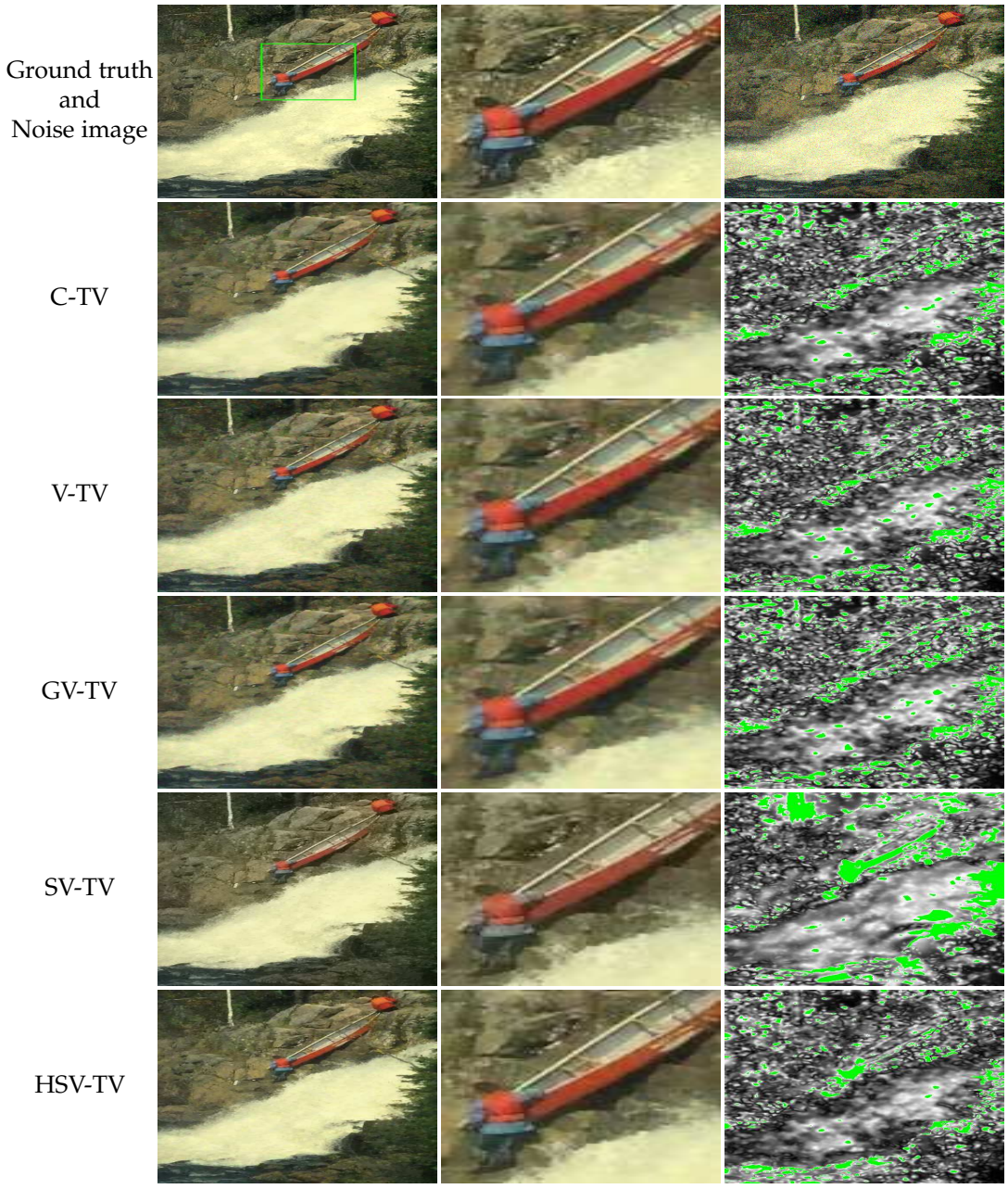

Figure 5: From left to right: The restored results of noisy level $\sigma = 0.1$, the corresponding zooming parts, and the spatial distribution of S-CIELAB error pixel (exceeding 5 units).

result and the ground-truth image by using the proposed HSV-TV model is the smallest among all the testing methods, which implies the effectiveness in color artifacts removing and saturation preserving.

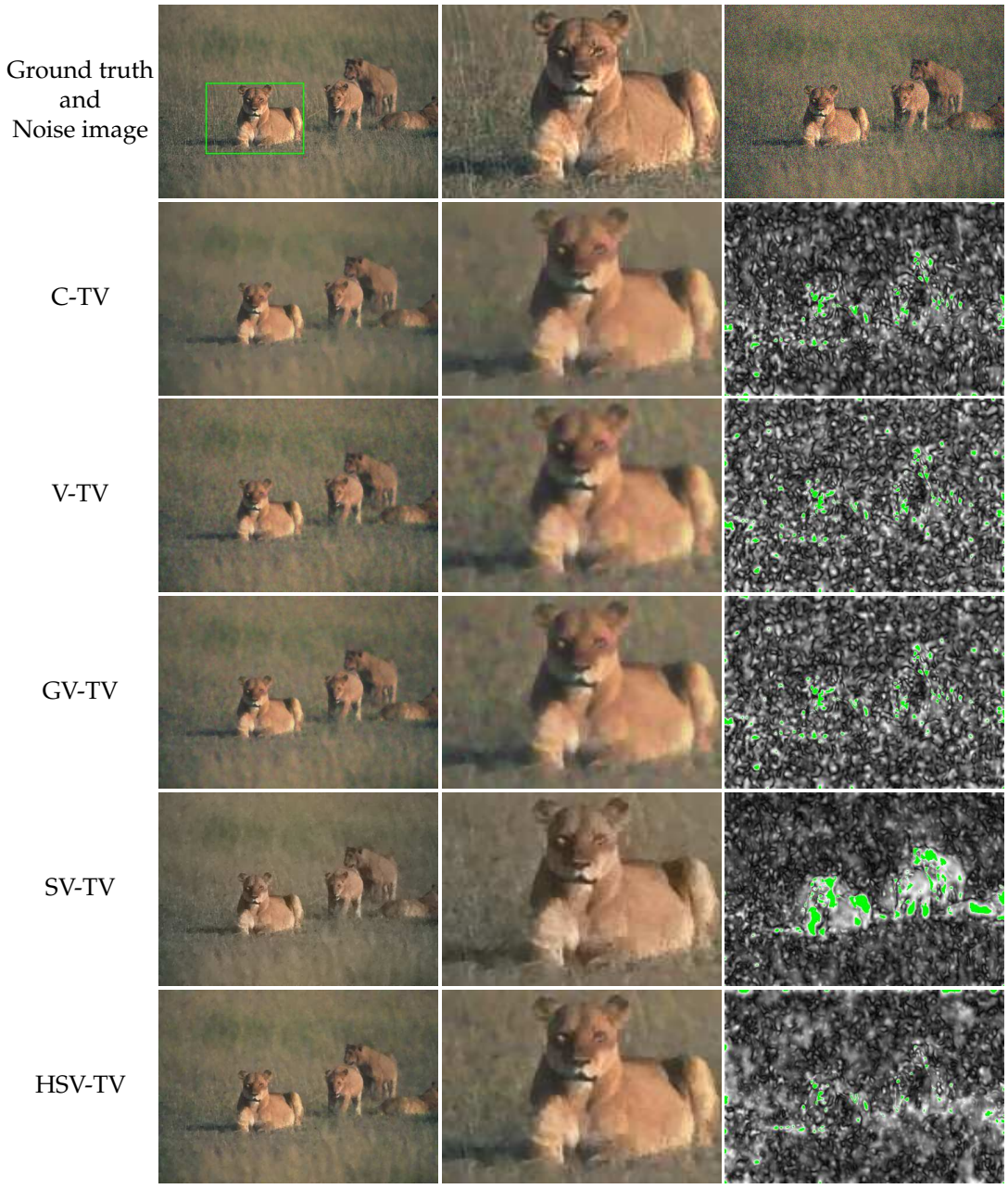

Figure 6: From left to right: The restored results of noisy level $\sigma = 0.1$, the corresponding zooming parts, and the spatial distribution of S-CIELAB error pixel (exceeding 5 units).

In Table 1, we present the measure values of the restored results in Figs. 4-7. The best values are marked in black. Meanwhile, we display the distributions of PSNR, SSIM values and the S-CIELAB color error values (pixel numbers exceeding 5 and 10 units)

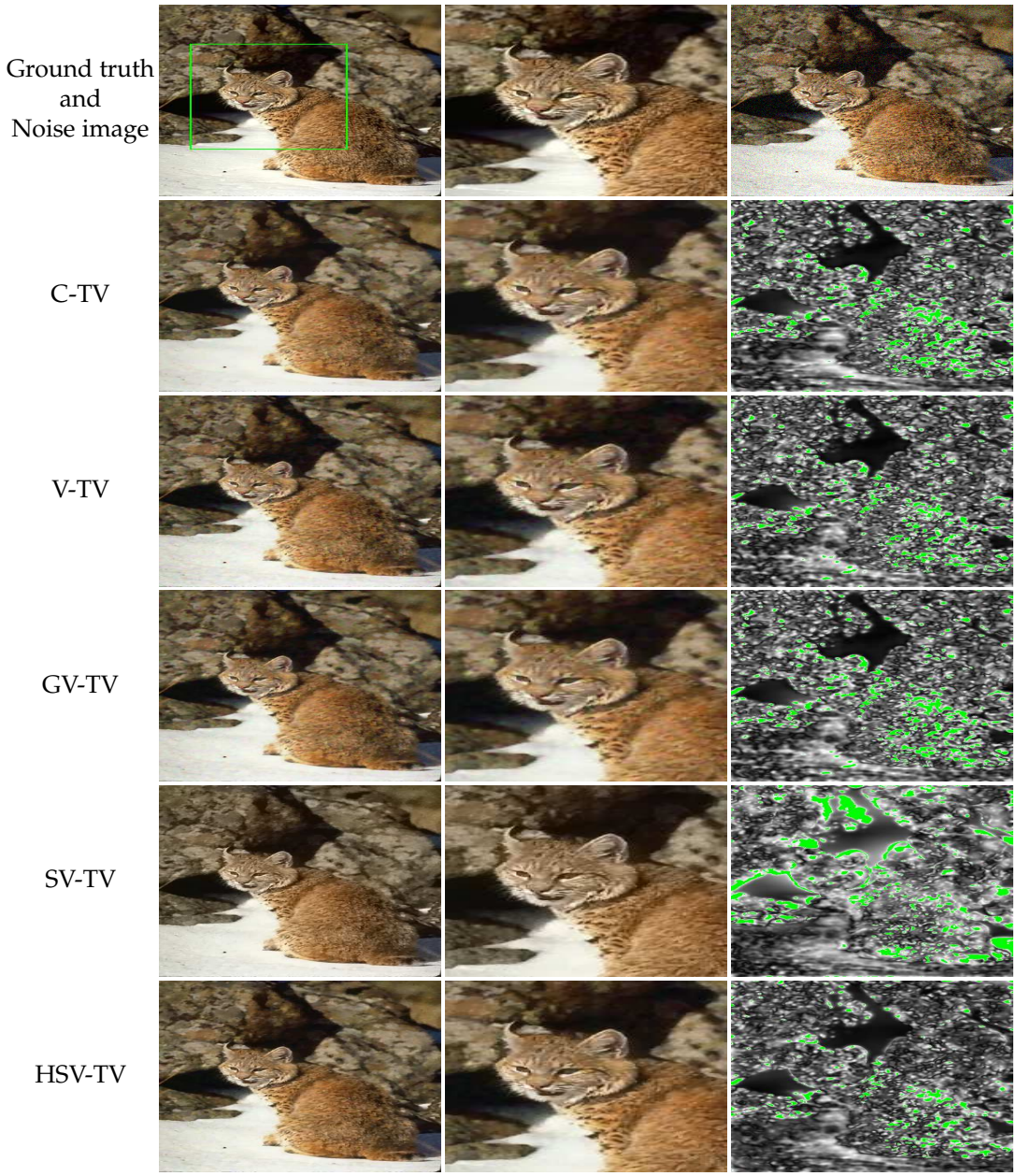

Figure 7: From left to right: The restored results of noisy level $\sigma = 0.1$, the corresponding zooming parts, and the spatial distribution of S-CIELAB error pixel (exceeding 5 units).

with respect to all 80 testing images in Fig. 8. The average measure values of different testing methods are shown in the corresponding labels. We see from Table 1 and Fig. 8 that the proposed model has the best results among all the testing methods for almost all the testing images in terms of all the testing measures.

Table 1: Measure values of the restored results ($\sigma=0.1$) by using different methods.

Fig.	Measure	Noisy image	C-TV	V-TV	GV-TV	SV-TV	HSV-TV
4	PSNR	20.3917	27.688	27.1395	27.5673	28.7029	**28.89**
	SSIM	0.6313	0.8908	0.8754	0.8868	0.9174	**0.9185**
	S-CIELAB Errors >5	46770	6378	7925	6937	8872	**4701**
	S-CIELAB Errors >10	12582	411	566	424	432	**310**
5	PSNR	20.3733	27.5302	26.9868	27.3925	28.4387	**28.6967**
	SSIM	0.6033	0.8609	0.8472	0.8577	0.891	**0.896**
	S-CIELAB Errors >5	66907	9451	9211	10145	17664	**7238**
	S-CIELAB Errors >10	17580	**372**	394	409	1659	419
6	PSNR	19.9927	31.42	30.644	31.2445	31.5805	**32.1896**
	SSIM	0.4039	0.9055	0.8822	0.8976	0.9121	**0.9191**
	S-CIELAB Errors >5	39844	1548	2115	1713	4204	**1148**
	S-CIELAB Errors >10	1392	59	74	63	13	**2**
7	PSNR	20.496	27.518	27.0498	27.4864	28.5372	**28.879**
	SSIM	0.5652	0.8836	0.8627	0.8759	0.8991	**0.9082**
	S-CIELAB Errors >5	48191	6482	5311	6767	10651	**3694**
	S-CIELAB Errors >10	6152	173	158	193	228	**66**

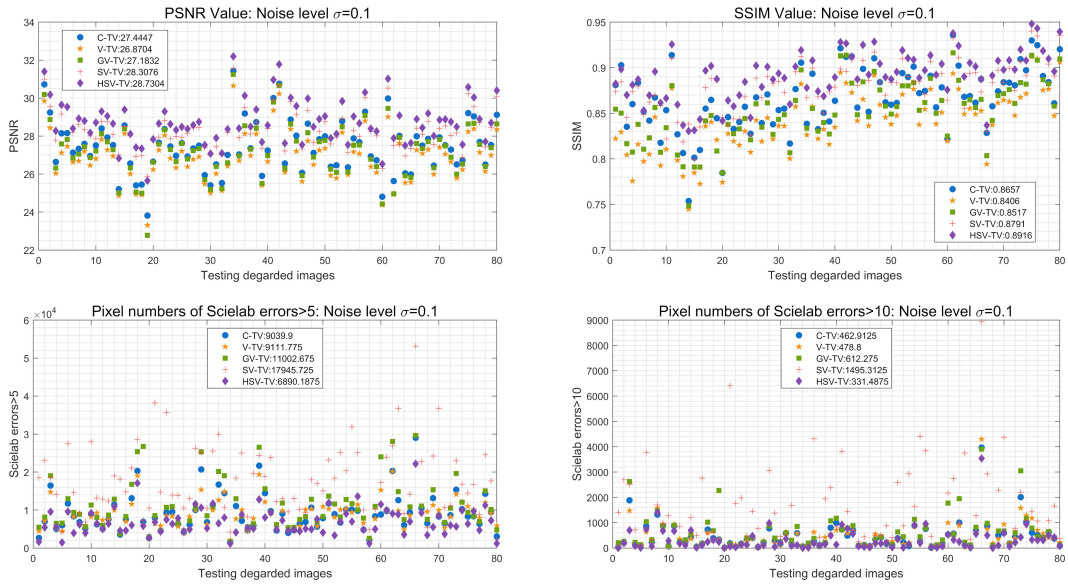

Figure 8: Distributions of measure values with respect to 80 testing images ($\sigma=0.1$).

5.2 Image denoising II: High noise level

In this experiment, we artificially add Gaussian noise of standard deviation 0.2 to degrade the ground-truth color images in each channel, and compute the PSNR, SSIM val-

ues and S-CIELAB error pixel numbers for each reconstruction by comparing it with the ground-truth image. By choosing the optimal value of the regularization parameter in terms of PSNR value for each testing method, we obtained the optimal restored result and the corresponding values of the measures.

As examples, we show several restored results in Figs. 9-12. We can clearly see from the output images that HSV-TV model and SV-TV model are more effective in handling color artifacts, see especially the color artifacts on the surface of the rock (Figs. 9 and 10), the ground (Fig. 11) and the leaves in the background (Fig. 12). Meanwhile, the proposed HSV-TV model is more effective in saturation retention compared with SV-TV model, see especially the high saturation parts of the restored results such as the red jacket and the boat (Fig. 9), the red coral (Fig. 10) and the yellow flower (Fig. 11).

Figure 9: Left: the ground truth image. Right (first row): the zoom-in parts of the noise image with noise level $\sigma = 0.2$, the restored results by using C-TV and V-TV respectively. Right (second row): the zoom-in parts of the restored results by using GV-TV, SV-TV and HSV-TV respectively.

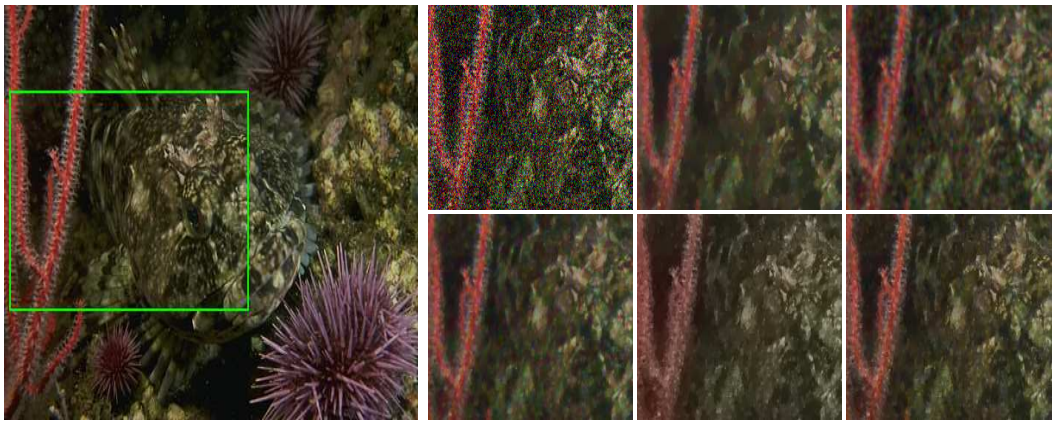

Figure 10: Left: the ground truth image. Right (first row): the zoom-in parts of the noise image with noise level $\sigma = 0.2$, the restored results by using C-TV and V-TV respectively. Right (second row): the zoom-in parts of the restored results by using GV-TV, SV-TV and HSV-TV respectively.

Figure 11: Left: the ground truth image. Right (first row): the zoom-in parts of the noise image with noise level $\sigma=0.2$, the restored results by using C-TV and V-TV respectively. Right (second row): the zoom-in parts of the restored results by using GV-TV, SV-TV and HSV-TV respectively.

Figure 12: Left: the ground truth image. Right (first row): the zoom-in parts of the noise image with noise level $\sigma=0.2$, the restored results by using C-TV and V-TV respectively. Right (second row): the zoom-in parts of the restored results by using GV-TV, SV-TV and HSV-TV respectively.

In Table 2, we present the measure values of the restored results in Figs. 9-12. The best values are marked in black. Meanwhile, we display the distributions of PSNR, SSIM values and the S-CIELAB color error values (pixel numbers exceeding 5, 10 and 15 units) with respect to all 80 testing images in Fig. 13. The average measure values of different testing methods are shown in the corresponding labels. We see from Table 2 and Fig. 13 that the proposed model has the best results among all the testing methods for almost all the testing images in terms of all the testing measures.

5.3 Image deblurring: Gaussian blur

In this experiment, we artificially convolute the ground truth image with a Gaussian kernel of standard deviation 1, and we then add Gaussian noise of standard deviation 0.1

Table 2: Measure values of the restored results ($\sigma=0.2$) by using different methods.

Fig.	Measure	Noisy image	C-TV	V-TV	GV-TV	SV-TV	HSV-TV
9	PSNR	14.941	24.4299	23.9359	24.2732	24.8753	**25.1743**
	SSIM	0.3199	0.7711	0.7437	0.7616	0.803	**0.8161**
	S-CIELAB Errors >5	148663	70478	74725	72627	81499	**59091**
	S-CIELAB Errors >10	100730	11551	13681	12175	14755	**7642**
	S-CIELAB Errors >15	58632	2165	2654	2209	3676	**1411**
10	PSNR	15.3771	23.3935	23.2483	23.441	23.8754	**24.2953**
	SSIM	0.2813	0.6969	0.6768	0.6917	0.7385	**0.7544**
	S-CIELAB Errors >5	152865	32631	34284	32088	49718	**20394**
	S-CIELAB Errors >10	124652	3009	3337	2627	6314	**645**
	S-CIELAB Errors >15	68396	183	240	150	602	**42**
11	PSNR	14.4099	23.294	22.8965	23.1388	24.2423	**24.2935**
	SSIM	0.3195	0.7393	0.7139	0.7262	0.7885	**0.7948**
	S-CIELAB Errors >5	138949	38442	42704	40301	37132	**31399**
	S-CIELAB Errors >10	67548	2658	3262	2897	2589	**1661**
	S-CIELAB Errors >15	22807	216	300	246	147	**121**
12	PSNR	14.8559	23.5464	23.0042	23.3671	24.2858	**24.6555**
	SSIM	0.3312	0.7949	0.7585	0.7671	0.8186	**0.8378**
	S-CIELAB Errors >5	138786	60091	66194	63709	67147	**42190**
	S-CIELAB Errors >10	103448	8626	11267	9751	8031	**4509**
	S-CIELAB Errors >15	68790	1427	1855	1689	1308	**754**

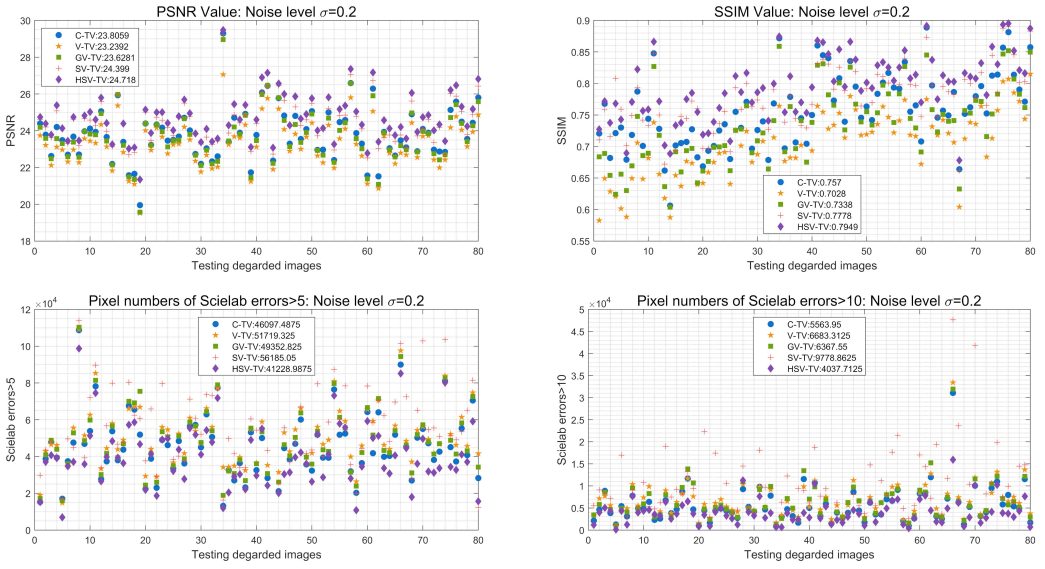

Figure 13: Distributions of measure values with respect to 80 testing images ($\sigma=0.2$).

to degrade the ground-truth color images in each channel, and compute the PSNR, SSIM values and S-CIELAB error pixel numbers for each restored result by comparing it with the ground-truth. By choosing the optimal value of the regularization parameter in terms of PSNR value for each testing method, we obtained the optimal restored result and the corresponding values of the measures.

As examples, we show several restored results (zoom-in parts of the restored results) in Fig. 14. Again we can clearly see from the output images that HSV-TV model and SV-TV model are more effective in handling color artifacts and detail recovery, see especially the texture structure of the rock and grass (Figs. 14(b)-14(d)). Meanwhile, the proposed HSV-TV model is more effective in saturation retention compared with SV-TV model, see especially the high saturation parts of the restored results such as the red jacket (Figs. 14(a) and 14(b)), the fur of the lion (Fig. 14(c)) and the cat (Fig. 14(d)).

In Table 3, we present the measure values of the restored results in Fig. 14. The best values are marked in black. Meanwhile, we also display the distributions of PSNR, SSIM values and the S-CIELAB color error values (pixel numbers exceeding 5 and 10 units) with respect to all 80 testing images in Fig. 15. The average measure values of different testing methods are shown in the corresponding labels. Again we see from Table 3 and Fig. 15 that the proposed model has the best results among all the testing methods for almost all the testing images in terms of all the testing measures.

5.4 Image deblurring: Motion blur

In the last experiment, we artificially convolute the ground truth image with a motion kernel of motion length 3 (Fig. 16(a)) or 5 (Fig. 16(b)) and motion angle 45. We then add Gaussian noise of standard deviation 0.1 and 0.2 to degrade the ground-truth color images in each channel, and compute the PSNR, SSIM values and S-CIELAB error pixel numbers for each restored result by comparing it with the ground-truth. By choosing the optimal value of the regularization parameter in terms of PSNR value for each testing method, we obtained the optimal restored result and the corresponding values of the measures.

As examples, we show several restored results (zoom-in parts of the restored results) in Fig. 16. Again we can clearly see from the output images that HSV-TV model and SV-TV model are more effective in handling color artifacts, see especially the surface of the rock and the texture structure of the sea urchin. Meanwhile, the proposed HSV-TV model is more effective in saturation retention compared with SV-TV model, see especially the high saturation parts of the restored results such as the red jacket, the red coral and the purple sea urchin.

In Table 4, we present the measure values of the restored results in Fig. 16. The best values are marked in black. We see from Table 4 that the proposed model has the best results among all the testing methods for all the testing images in terms of all the testing measures.

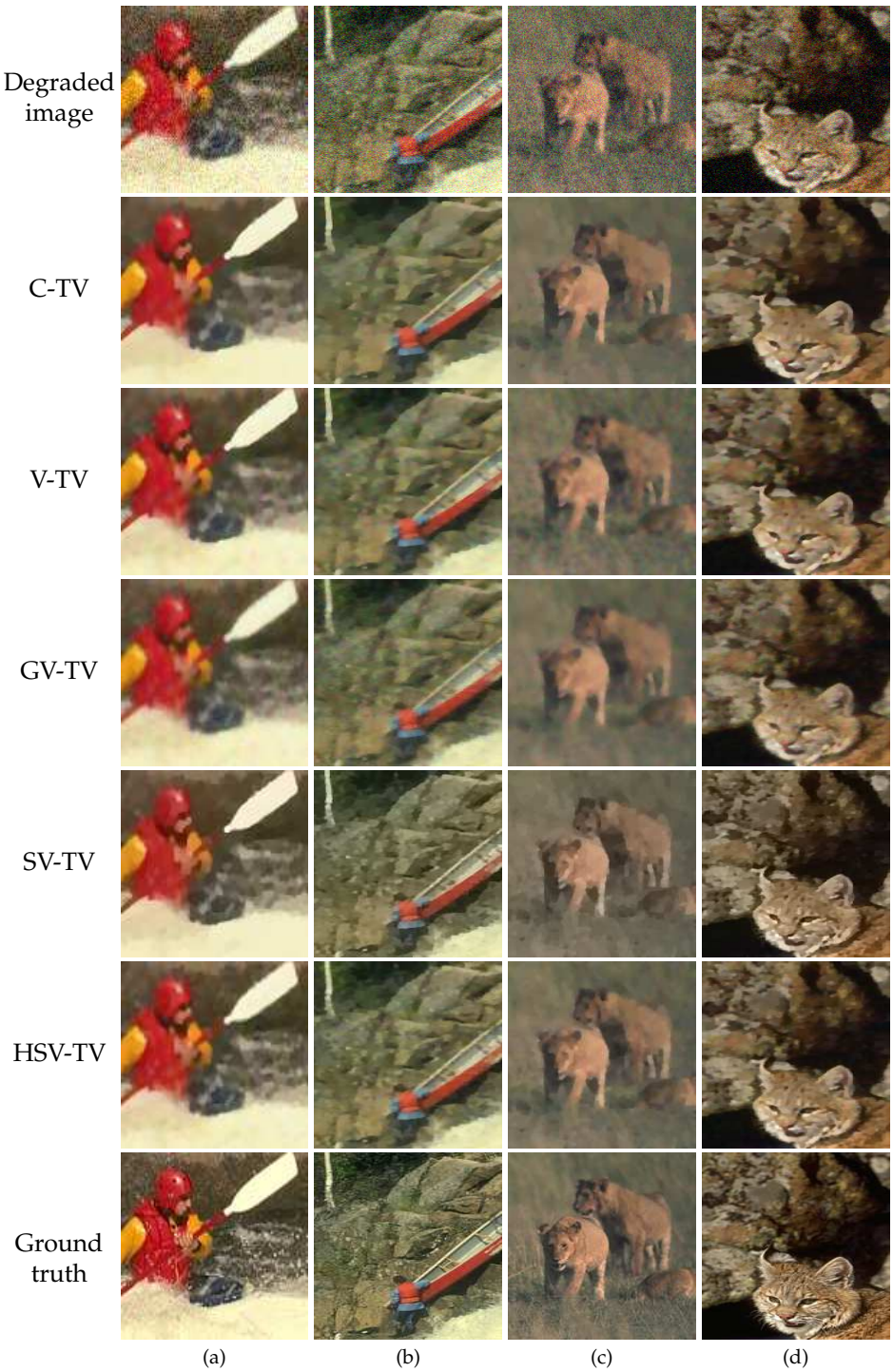

Figure 14: The corresponding zoom-in parts of the restored results of Gaussian blur level $\sigma=1$ and noise level $\sigma=0.1$.

Table 3: Measure values of the restored results (Gaussian blur) by using different methods.

Measure	Methods	Fig. 14a	Fig. 14b	Fig. 14c	Fig. 14d
PSNR	C-TV	25.6307	25.62	30.4293	25.4641
	V-TV	25.4927	25.4976	29.8058	25.381
	GV-TV	25.2857	25.1973	30.0394	25.0932
	SV-TV	25.8325	26.0975	30.2892	25.7529
	HSV-TV	**26.3196**	**26.2082**	**30.7693**	**26.4486**
	Noisy image	19.6457	19.6919	19.8119	19.8131
SSIM	C-TV	0.8442	0.799	0.8878	0.8525
	V-TV	0.8365	0.7927	0.869	0.8378
	GV-TV	0.8313	0.7865	0.8837	0.831
	SV-TV	0.8553	0.8244	0.8882	0.8671
	HSV-TV	**0.8625**	**0.8252**	**0.8949**	**0.8733**
	Noisy image	0.5576	0.5164	0.3733	0.5158
S-CIELAB Errors >5	C-TV	13188	19026	3817	17422
	V-TV	13264	18212	5193	16065
	GV-TV	16377	20199	5506	20430
	SV-TV	13474	16029	4030	**10558**
	HSV-TV	**9038**	**13717**	**1999**	10765
	Noisy image	41842	53693	34474	39805
S-CIELAB Errors >10	C-TV	2174	2161	196	2056
	V-TV	2151	1933	264	1848
	GV-TV	2246	2308	238	2519
	SV-TV	1440	1392	62	**799**
	HSV-TV	**915**	**1071**	**61**	892
	Noisy image	9288	11193	1535	4831

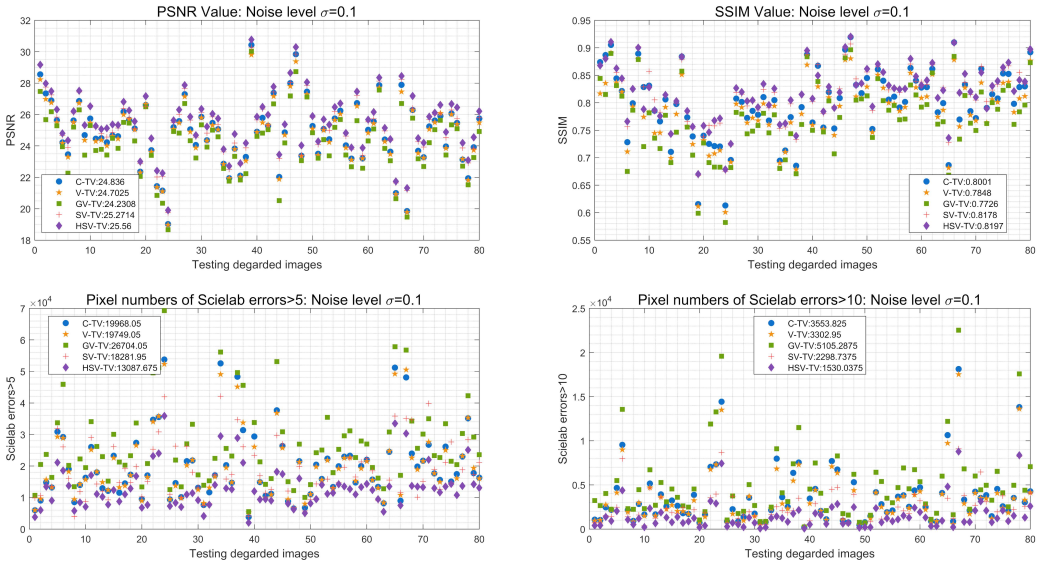

Figure 15: Distributions of measure values with respect to 80 testing images of Gaussian deblurring experiment.

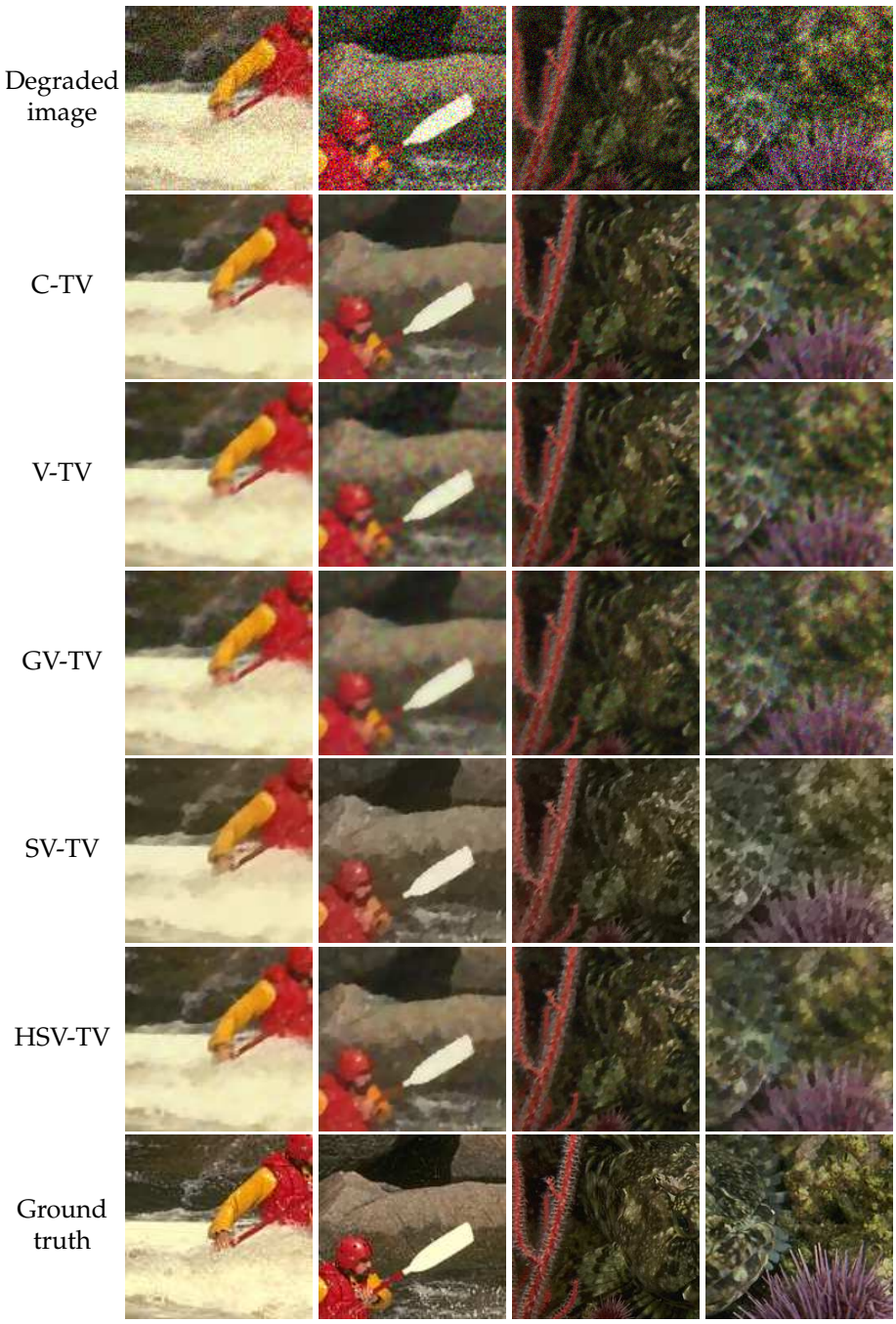

Figure 16: The corresponding zoom-in parts of the restored results by using different methods. First column (image a): the restored results of Motion blur with $len=3$ and noise level $\sigma=0.1$; Second column (image a): the restored results of Motion blur with $len=3$ and noise level $\sigma=0.2$; Third column (image b): the restored results of Motion blur with $len=5$ and noise level $\sigma=0.1$; Fourth column (image b): the restored results of Motion blur with $len=5$ and noise level $\sigma=0.2$.

Table 4: Measure values of the restored results (Motion blur) by using different methods.

Measure	Methods	Fig. 16(a)		Fig. 16(b)	
PSNR	C-TV	26.2449	24.1587	24.8261	22.6891
	V-TV	25.9759	23.7442	24.5871	22.5672
	GV-TV	25.9171	23.9069	24.2353	22.3864
	SV-TV	26.4253	24.5276	25.1367	22.9548
	HSV-TV	**27.0619**	**24.723**	**25.3245**	**23.0126**
	Noisy image	19.8809	14.7722	19.585	15.0001
SSIM	C-TV	0.8591	0.8007	0.7668	0.6524
	V-TV	0.8459	0.7728	0.7498	0.632
	GV-TV	0.8472	0.7902	0.7346	0.6242
	SV-TV	0.8673	0.8243	0.7866	0.6814
	HSV-TV	**0.8789**	**0.8276**	**0.7917**	**0.683**
	Noisy image	0.5795	0.3078	0.4315	0.2103
S-CIELAB Errors >5	C-TV	10960	54118	21470	39113
	V-TV	12699	61112	27394	42844
	GV-TV	12995	59024	34732	43220
	SV-TV	14787	50563	26135	49943
	HSV-TV	**7487**	**42082**	**15550**	**36496**
	Noisy image	41492	135420	53878	148755
S-CIELAB Errors >10	C-TV	1275	4872	2879	5403
	V-TV	1665	6772	3604	6164
	GV-TV	1496	6133	5377	6411
	SV-TV	873	3959	1725	5410
	HSV-TV	**711**	**3072**	**1444**	**4327**
	Noisy image	9559	63387	4393	116699

Meanwhile, we make use of the examples in Fig. 16 to show the energy curves with respect to iterations in Fig. 17. We see from the curves that the proposed algorithm converges in about 150 iterations for low noise level ($\sigma = 0.1$), and converges in about 250 iterations for high noise level ($\sigma = 0.2$), which demonstrates the effectiveness of the proposed algorithm.

6 Concluding remarks

As a summary, we have proposed a novel hue-saturation-value total variation regularization and a corresponding color image restoration model. We give a detailed derivation about the hue, saturation, and value components of a color image in the quaternion framework based on the geometric meaning. Meanwhile, we study the dual formula-

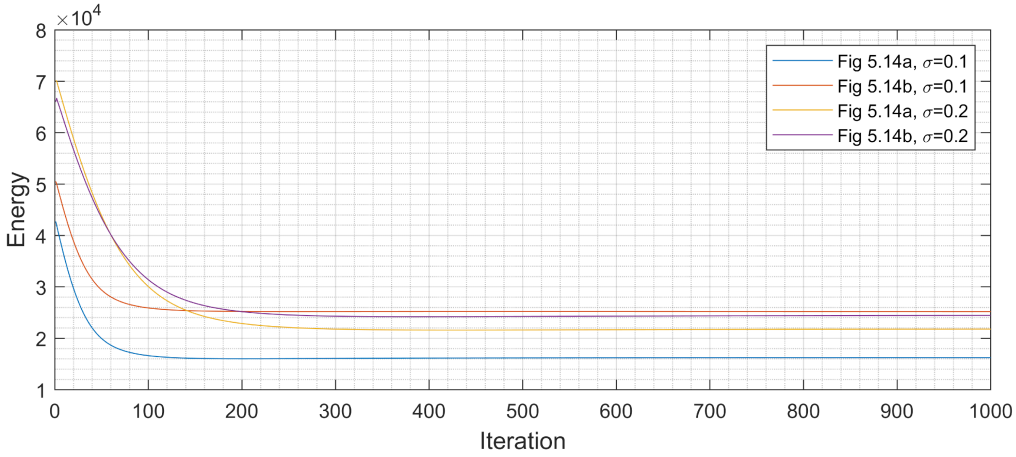

Figure 17: The energy curves with respect to iterations.

tion, lower semi-continuity, approximation and compactness properties of the proposed HSV-TV regularization. We then develop a color image restoration model and study the existence of the minimizer of the proposed minimization problem. Numerically we give an efficient algorithm to solve the proposed minimization problem, and we show the convergence of the proposed algorithm. Numerical results have demonstrated that the performance of the proposed HSV-TV regularization and the proposed color image restoration model is better than that of other testing methods.

Appendix A

We have defined H_r, H_g, and H_b in (3.15), we then give the detailed calculations as follows:

$$\begin{aligned}
\begin{bmatrix} H_r \\ H_g \\ H_b \end{bmatrix} &= \frac{\partial H(\mathbf{u})}{\partial \mathbf{u}} = \frac{1}{1+(\|\mathbf{C_1u}\|/\|\mathbf{C_2u}\|)^2} \frac{\partial(\|\mathbf{C_1u}\|/\|\mathbf{C_2u}\|)}{\partial \mathbf{u}} \\
&= \frac{1}{1+(\|\mathbf{C_1u}\|/\|\mathbf{C_2u}\|)^2} \left(\frac{\|\mathbf{C_2u}\| \partial(\|\mathbf{C_1u}\|)/\partial \mathbf{u} - \|\mathbf{C_1u}\| \partial(\|\mathbf{C_2u}\|)/\partial \mathbf{u}}{\|\mathbf{C_2u}\|^2} \right) \\
&= \frac{1}{\|\mathbf{C_1u}\|^2+\|\mathbf{C_2u}\|^2} \left(\frac{\|\mathbf{C_2u}\| \mathbf{C_1}^T(\mathbf{C_1u})}{\|\mathbf{C_1u}\|} - \frac{\|\mathbf{C_1u}\| \mathbf{C_2}^T(\mathbf{C_2u})}{\|\mathbf{C_2u}\|} \right) \\
&= \frac{1}{\|\mathbf{Cu}\|^2} \left(\|\mathbf{C_2u}\| \frac{\mathbf{C_1u}}{\|\mathbf{C_1u}\|} - \|\mathbf{C_1u}\| \frac{\mathbf{C_2u}}{\|\mathbf{C_2u}\|} \right),
\end{aligned}$$

where

$$\|\mathbf{C_1u}\| = \frac{|u_g - u_b|}{\sqrt{2}} = \frac{\beta_2(u_g - u_b)}{\sqrt{2}},$$

$$\frac{\mathbf{C_1u}}{\|\mathbf{C_1u}\|}=\frac{\beta_2}{\sqrt{2}}\begin{bmatrix}0\\1\\-1\end{bmatrix},$$
$$\|\mathbf{C_2u}\|=\frac{|2u_r-u_g-u_b|}{\sqrt{6}}=\frac{\beta_1(2u_r-u_g-u_b)}{\sqrt{6}},$$
$$\frac{\mathbf{C_2u}}{\|\mathbf{C_2u}\|}=\frac{\beta_1}{\sqrt{6}}\begin{bmatrix}2\\-1\\-1\end{bmatrix}.$$

Therefore, we have

$$\|\mathbf{C_2u}\|\frac{\mathbf{C_1u}}{\|\mathbf{C_1u}\|}=\frac{\beta_1\beta_2}{2\sqrt{3}}\begin{bmatrix}0\\2u_r-u_g-u_b\\-2u_r+u_g+u_b\end{bmatrix},$$
$$\|\mathbf{C_1u}\|\frac{\mathbf{C_2u}}{\|\mathbf{C_2u}\|}=\frac{\beta_1\beta_2}{2\sqrt{3}}\begin{bmatrix}2u_g-2u_b\\-u_g+u_b\\-u_g+u_b\end{bmatrix},$$
$$\frac{\partial \mathrm{H}(\mathbf{u})}{\partial \mathbf{u}}=\frac{\beta_1\beta_2}{\sqrt{3}\|\mathbf{Cu}\|^2}\begin{bmatrix}u_b-u_g\\u_r-u_b\\u_g-u_r\end{bmatrix},$$

which gives that

$$\mathrm{H_r}=\beta_1\beta_2\frac{u_b-u_g}{\sqrt{3}\|\mathbf{Cu}\|^2},\quad \mathrm{H_g}=\beta_1\beta_2\frac{u_r-u_b}{\sqrt{3}\|\mathbf{Cu}\|^2},\quad \mathrm{H_b}=\beta_1\beta_2\frac{u_g-u_r}{\sqrt{3}\|\mathbf{Cu}\|^2}.$$

Acknowledgments

W. Wang is supported by the Natural Science Foundation of Shanghai (Grant No. 22ZR1465300).

References

[1] T. Azetsu and N. Suetake, *Hue-preserving image enhancement in cielab color space considering color gamut*, Opt. Rev., 26:283–294, 2019.
[2] P. Blomgren and T. F. Chan, *Color TV: Total variation methods for restoration of vector-valued images*, IEEE Trans. Image Process., 7(3):304–309, 1998.
[3] L. M. Bregman, *The relaxation method of finding the common point of convex sets and its application to the solution of problems in convex programming*, USSR Comput. Math. Math. Phys., 7(3):200–217, 1967.
[4] X. Bresson and T. F. Chan, *Fast dual minimization of the vectorial total variation norm and applications to color image processing*, Inverse Probl. Imaging, 2(4):455–484, 2008.
[5] K. R. Castleman, *Digital Image Processing*, Prentice Hall Press, 1996.

[6] A. Chambolle, *An algorithm for total variation minimization and applications*, J. Math. Imaging Vision, 20:89–97, 2004.
[7] T. F. Chan, G. H. Golub, and P. Mulet, *A nonlinear primal-dual method for total variation-based image restoration*, SIAM J. Sci. Comput., 20:1964–1977, 1999.
[8] T. F. Chan, S. H. Kang, and J. Shen, *Total variation denoising and enhancement of color images based on the CB and HSV color models*, J. Vis. Commun. Image Represent., 12(4):422–435, 2001.
[9] A. M. Chaudhry, M. M. Riaz, and A. Ghafoor, *A framework for outdoor RGB image enhancement and dehazing*, IEEE Geosci. Remote Sens. Lett., 15:932–936, 2018.
[10] T.-W. Chen, Y.-L. Chen, and S.-Y. Chien, *Fast image segmentation based on K-Means clustering with histograms in HSV color space*, in: 2008 IEEE 10th Workshop on multimedia signal processing, IEEE, 322–325, 2008.
[11] P. Denis, P. Carré, and C. Fernandez-Maloigne, *Spatial and spectral quaternionic approaches for colour images*, Comput. Vis. Image Underst., 107:74–87, 2007.
[12] S. Di Zenzo, *A note on the gradient of a multi-image*, Comput. Graph. Image Process., 33:116–125, 1986.
[13] J. Duran, M. Moeller, C. Sbert, and D. Cremers, *Collaborative total variation: A general framework for vectorial TV models*, SIAM J. Imaging Sci., 9:116–151, 2016.
[14] S. Esedoğlu and S. J. Osher, *Decomposition of images by the anisotropic Rudin-Osher-Fatemi model*, Comm. Pure Appl. Math., 57(12):1609–1626, 2004.
[15] A. Galdran, J. Vazquez-Corral, D. Pardo, and M. Bertalmio, *Enhanced variational image dehazing*, SIAM J. Imaging Sci., 8:1519–1546, 2015.
[16] G. Gilboa and S. Osher, *Nonlocal linear image regularization and supervised segmentation*, Multiscale Model. Simul., 6:595–630, 2007.
[17] B. Goldluecke, E. Strekalovskiy, and D. Cremers, *The natural vectorial total variation which arises from geometric measure theory*, SIAM J. Imaging Sci., 5:537–563, 2012.
[18] M. R. Hestenes, *Multiplier and gradient methods*, J. Optim. Theory Appl., 4:303–320, 1969.
[19] C. Huang, M. K. Ng, T. Wu, and T. Zeng, *Quaternion-based dictionary learning and saturation-value total variation regularization for color image restoration*, IEEE Trans. Multimedia, 24:3769–3781, 2021.
[20] Z.-K. Huang and D.-H. Liu, *Segmentation of color image using EM algorithm in HSV color space*, in: 2007 International Conference on Information Acquisition, IEEE, 316–319, 2007.
[21] Z. Jia, M. K. Ng, and W. Wang, *Color image restoration by saturation-value total variation*, SIAM J. Imaging Sci., 12(2):972–1000, 2019.
[22] L. Jin and D. Li, *A switching vector median filter based on the CIELAB color space for color image restoration*, Signal Processing, 87(6):1345–1354, 2007.
[23] M. Jung, *Saturation-value based higher-order regularization for color image restoration*, Multidim. Syst. Sign. Process., 34(2):365–394, 2023.
[24] D. Martin, C. Fowlkes, D. Tal, and J. Malik, *A database of human segmented natural images and its application to evaluating segmentation algorithms and measuring ecological statistics*, in: Proceedings Eighth IEEE International Conference on Computer Vision. ICCV 2001, IEEE, Vol. 2, 416–423, 2001.
[25] S. Ono and I. Yamada, *Decorrelated vectorial total variation*, in: Proceedings of the IEEE Conference on Computer Vision and Pattern Recognition, 4090–4097, 2014.
[26] F. Petit, A.-S. Capelle-Laizé, and P. Carré, *Hue-based quaternionic criterion for focused-color extraction*, in: 2010 IEEE International Conference on Image Processing, IEEE, 1617–1620, 2010.
[27] R. T. Rockafellar, *A dual approach to solving nonlinear programming problems by unconstrained optimization*, Math. Program., 5:354–373, 1973.

[28] P. Rodriguez and B. Wohlberg, *A generalized vector-valued total variation algorithm*, in: 2009 16th IEEE International Conference on Image Processing (ICIP), IEEE, 1309–1312, 2009.
[29] L. I. Rudin, S. Osher, and E. Fatemi, *Nonlinear total variation based noise removal algorithms*, Phys. D, 60:259–268, 1992.
[30] G. Sapiro, *Vector-valued active contours*, in: Proceedings CVPR IEEE Computer Society Conference on Computer Vision and Pattern Recognition, IEEE, 680–685, 1996.
[31] W. Wang, F. Li, and M. K. Ng, *Structural similarity-based nonlocal variational models for image restoration*, IEEE Trans. Image Process., 28:4260–4272, 2019.
[32] W. Wang and M. K. Ng, *Color image restoration by saturation-value total variation regularization on vector bundles*, SIAM J. Imaging Sci., 14:178–197, 2021.
[33] W. Wang, Y. Yang, and M. K. Ng, *A spatial color compensation model using saturation-value total variation*, SIAM J. Imaging Sci., 15:1400–1430, 2022.
[34] W. Wang, M. Yao, and M. K. Ng, *Color image multiplicative noise and blur removal by saturation-value total variation*, Appl. Math. Model., 90:240–264, 2021.
[35] Z. Wang, A. C. Bovik, H. R. Sheikh, and E. P. Simoncelli, *Image quality assessment: From error visibility to structural similarity*, IEEE Trans. Image Process., 13:600–612, 2004.
[36] Y.-W. Wen, M. K. Ng, and Y.-M. Huang, *Efficient total variation minimization methods for color image restoration*, IEEE Trans. Image Process., 17:2081–2088, 2008.
[37] Y.-W. Wen, M. Zhao, and M. Ng, *Cartoon and texture decomposition for color image in opponent color space*, Appl. Math. Comput., 414:126654, 2022.
[38] C. Wu and X.-C. Tai, *Augmented Lagrangian method, dual methods, and split Bregman iteration for ROF, vectorial TV, and high order models*, SIAM J. Imaging Sci., 3(3):300–339, 2010.
[39] T. Wu, Z. Mao, Z. Li, Y. Zeng, and T. Zeng, *Efficient color image segmentation via quaternion-based L_1/L_2 regularization*, J. Sci. Comput., 93(1):9, 2022.
[40] X. Zhang and B. A. Wandell, *A spatial extension of CIELAB for digital color-image reproduction*, in: SID International Symposium Digest of Technical Papers, Citeseer, Vol. 27, 731–734, 1996.